Article

Exploiting the role of molecular electrostatic potential, deformation density, topology and energetics in the characterization of S···N and Cl···N supramolecular motifs in crystalline triazolothiadiazoles

Imtiaz Khan, Piyush Panini, Salah Ud-Din Khan, Usman Ali Rana, Hina Andleeb, Deepak Chopra, Shahid Hameed, and Jim Simpson

Cryst. Growth Des., **Just Accepted Manuscript** • DOI: 10.1021/acs.cgd.5b01499 • Publication Date (Web): 12 Jan 2016

Exploiting the role of molecular electrostatic potential, deformation density, topology and energetics in the characterization of S···N and Cl···N supramolecular motifs in crystalline triazolothiadiazoles

Imtiaz Khan[a], Piyush Panini[b], Salah Ud-Din Khan[c], Usman Ali Rana[c], Hina Andleeb[a], Deepak Chopra[b,], Shahid Hameed[a,]*, Jim Simpson[d,]**

[a]Department of Chemistry, Quaid-i-Azam University, Islamabad-45320, Pakistan

[b]Crystallography and Crystal Chemistry Laboratory, Department of Chemistry, IISER, Bhopal 462066, India

[c]Deanship of Scientific Research, College of Engineering, King Saud University, PO Box 800, Riyadh 11421, Saudi Arabia

[d]Department of Chemistry, University of Otago, P.O. Box 56, Dunedin, 9054, New Zealand

**Corresponding authors. E-mail: dchopra@iiserb.ac.in (D.Chopra); Tel.: +91-07556692370; Fax: +91-07556692392; E-mail: shameed@qau.edu.pk (S. Hameed); Tel.: +92 51 9064 2133; Fax: +92 51 2241; E-mail: jsimpson@alkali.otago.ac.nz (J. Simpson) Tel: +64 3 479 7914; Fax: +64 3 479 7906;*

Abstract

A detailed analysis of the molecular and crystal packing of a series of pharmaceutically active triazolothiadiazole derivatives is reported. The most notable feature from the analysis of the supramolecular motifs is the presence of inversion dimers due to the formation of strong S···N chalcogen bonds. This has been unequivocally established *via* inputs from energy calculations from PIXEL, the topological analysis using the approach of QTAIM from AIMALL, an analysis of the molecular electrostatic potentials plotted on Hirshfeld surfaces and the analysis of the 3D-deformation densitities obtained using Crystal Explorer. The total interaction energy for this contact is in the range of 28-33 kJ/mol in the molecules under investigation and the electrostatic (Coulombic + polarization) contribution towards the total stabilization energy is more than 70% indicating that such interactions are principally electrostatic in origin.The results from the analysis of the molecular ESP depicts that this interaction exists between a strongly electropositive σ-hole on the sulfur atom with an electronegative region on the nitrogen. 3D-deformation density (DD) maps reveals the presence of a charge depletion (CD) region on the sulfur atom which is directed towards the charge concentration (CC) region on the nitrogen atom facilitating formation of such contacts in the crystal. These are further invesigated by QTAIM based calculations which establish the closed-shell nature of these contacts. The crystal packing is further stabilized by the presence of significantly important π...π stacking interactions, wherein the interaction energies, calculated by the PIXEL method, reveal that some of these interactions in crystals have significant contributions from electrostatic components, with a lesser contribution from dispersion forces that normally dominate such interactions. The existence of a contribution of ~48% from electrostatics between stacked rings owing to their unique electrostatic complementarity is a rare supramolecular feature observed in crystal packing in these solids. In addition, the existence of C-H···O, C-H···N, C-H···F, Cl···N interactions are also characterized by a significant electrostatic component in their formation in crystals of these compounds.

1. Introduction

Intermolecular interactions play a very essential role in many branches of science including molecular recognition and aggregation, crystal engineering, polymorphism. They also have great importance in biochemistry and structural biology[1-4]. It is a very important tool to understand such interactions when designing a material with specific desirable properties[5-6]. Hence, the study of different intermolecular interactions has always been a fascinating area of research in science. In general, the primary focus of the study of intermolecular interactions has been on the conventional hydrogen bond (e.g., NH···O and OH···O) and its utilization in the design of required supramolecular structures[6]. Increasingly, however, the importance of the weak hydrogen bond, C-H···X (X= N, O, halogens, π electrons) has also been realized in different areas[7-11] and the nature and characteristics of such interactions is now very well understood[12-13].

In recent years, attention has shifted towards the study of other classes of intermolecular interaction such as π···π contacts[14], lp···π interactions[15-17], halogen bonds[18-19], chalcogen bonds[20-25] etc. π···π interactions were found to be important in biological molecules like DNA, proteins and other important functional materials of organic origin[14]. A recently recognized class of interactions are those between the charge depleted (CD) region, known as a σ-hole[26-29], on an atom (mainly involving atoms of groups IV−VII in the periodic table) with the charge concentrated (CC) region of an atom or part of a molecule, such as a π-ring. Amongst these, the most commonly investigated interaction is the "halogen bond", which involves an interaction of the CD region on a halogen atom, opposite to a sigma bond, with the other, non-hydrogen atoms in the molecule. According to the recent IUPAC definition[30], "*A halogen bond occurs when there is evidence of a net attractive interaction between an electrophilic region associated with a halogen atom in a molecular entity and a nucleophilic region in another, or the same, molecular entity*". One of the characteristic features associated with this interaction, similar to that of the hydrogen bond, is that these are highly "directional" and the strength depends very much on the magnitude of the CD region on the halogen atom.

Moreover, carbon bonds[31], pincogen bonds[32-33] (Group V elements) and chalcogen bonds[20-25] (Group VI elements) are similar interactions that also involve the presence of a σ-hole. These are currently a prime research focus so that such contacts can be used effectively to construct supramolecular assemblies. Furthermore, their importance has been widely recognized in

different areas, including chemical biology, drug design, and functional organic materials research[18-33].

Recognizing the importance of the above-mentioned interactions, in the present study, a series of five pharmaceutically active triazolothiadiazole derivatives have been synthesized and their crystal structures have been investigated by single crystal X-Ray diffraction. The packing of molecules in the crystal involve important supramolecular interactions and the nature and properties of these have been quantitatively investigated with contributions from different computational approaches. For the current study, the heterocycles and aromatic systems that make up the molecules were choosen because they occur in numerous structurally diverse bioactive natural products, synthetic drugs and pharmaceuticals. Such drug candidates drug candidates find widespread applications in medicinal chemistry, and have gained eminence due to their substantial therapeutic potential for the effective treatment of various disorders[34-35]. Amongst them, conjugated heterocycles derived from the 1,2,4-triazole scaffold are particularly special heterocyclic ring systems featured in a large number of compounds with diverse and important biological activities. These hybrid structures have been observed in a wide variety of therapeutically important compounds demonstrating a broad spectrum of biological functions including use as antitumor, antiviral, antihelmintic, antifungal, antibacterial, antitubercular, anti-inflammatory or analgesic agents and as CNS-stimulants, PDE4 inhibitors or hypoglycemic agents[36-45]. In addition, triazolothiadiazoles have also been identified as selective inhibitors of the c-Met proteins[46] and are used as molluscicidal agents[47], growth promoters[48], or as cholinesterase, monoamine oxidase, alkaline phosphatase and urease inhibitors[49].

2. Experimental

2.1. General

All commercially available reagents were used as received. Thin layer chromatography (TLC) was performed on Merck DF-Alufoilien $60F_{254}$ 0.2 mm precoated plates. Product spots were visualized under UV light at 254 and 365 nm. Melting points were recorded on a Stuart melting point apparatus (SMP3) and are uncorrected. Infra-red (IR) spectra were recorded on FTS 3000 MX, Bio-Rad Merlin (Excalibur model) spectrophotometer. ^{1}H NMR spectra were recorded on a Bruker Avance (300 MHz) spectrometer. Chemical shifts (δ) are quoted in parts per million (ppm) downfield of tetramethylsilane, using residual protonated solvent as internal standard (DMSO-d_6 at 2.50 ppm). Proton-decoupled ^{13}C NMR spectra were recorded on a Bruker Avance

(75 MHz) spectrometer using deuterated solvent as internal standard (DMSO-d_6 at 39.52 ppm). The elemental analysis was performed on Leco CHNS-932 Elemental Analyzer, Leco Corporation (USA).

2.2. Preparation of triazolothiadiazoles

2.2.1. General procedure for the synthesis of 4-amino-1,2,4-triazole-3-thiols (3a-c)

The appropriate carbohydrazide (**1a-c**) (1.0 mmol) was stirred with a solution of potassium hydroxide (1.5 mmol) dissolved in methanol (10 mL) at 0-5 °C. Carbon disulfide (1.5 mmol) was added slowly to this solution and the reaction mixture was left overnight at room temperature. The solid potassium dithiocarbazinate product (**2a-c**) was filtered, washed with chilled methanol and dried. It was used directly for next step without further purification.

To a solution of the corresponding potassium dithiocarbazinate (**2a-c**) in water (8 mL), hydrazine hydrate (2.0 mmol) was added and the reaction mixture was refluxed for 4-5 h. During progress of the reaction, the mixture turned green with the evolution of hydrogen sulphide and finally became homogeneous. It was then diluted with little cold water and acidified with conc. hydrochloric acid. The white precipitated solid was filtered, washed with cold water and recrystallized from aqueous ethanol to afford the compounds (**3a-c**). The physical and spectroscopic data obtained were found to be consistent with those observed in literature[48, 50-51].

2.2.2. General procedure for the synthesis of 1,2,4-triazolo[3,4-*b*][1,3,4]thiadiazoles (4a-e)

A mixture of the corresponding 4-amino-1,2,4-triazole-3-thiol (**3a-c**) (1.0 mmol) and the substituted aromatic/hetero-aromatic acids (1.1 mmol) in $POCl_3$ (5 mL) was refluxed for 6 h. The reaction mixture was slowly poured into crushed ice with stirring and neutralized with sodium bicarbonate. The precipitated mass was filtered, washed with cold water, dried, and recrystallized (ethanol) to afford the 1,2,4-triazolo[3,4-*b*][1,3,4]thiadiazoles **(4a-e)** [48, 50-51]. The synthesis of compound **4d** has been reported by us previously[52], and the spectroscopic data obtained for **4a** were found to be consistent with those observed in literature[48].

2.2.1.1. 6-(2-Chloro-4,5-difluorophenyl)-3-(pyridin-3-yl)-[1,2,4]triazolo[3,4-*b*][1,3,4]thiadiazole (4b)

Off-white solid (79%): m.p 147-148 ^{o}C; R_f: 0.65 (10% MeOH/$CHCl_3$); IR (ATR, cm^{-1}): 3015 (Ar-H), 1593 (C=N), 1572, 1499 (C=C) 1168 (C-F), 1023 (C-Cl); ^{1}H NMR (300 MHz, DMSO-d_6): δ 9.39 (s, 1H, Ar-H), 8.74 (d, 1H, J = 6.9 Hz, Ar-H), 8.56-8.52 (m, 1H, Ar-H), 8.41-8.35 (m, 1H, Ar-H), 8.15-8.14 (m, 1H, Ar-H), 8.14-8.08 (m, 1H, Ar-H); ^{13}C NMR (75 MHz, DMSO-d_6): δ 170.89, 163.55, 159.74, 156.82, 151.26, 148.43, 147.54, 144.09, 137.39, 135.67, 132.63, 131.24, 126.89, 121.27, 120.99, 119.99. Analysis Calcd for $C_{14}H_6ClF_2N_5S$: C, 48.08; H, 1.73; N, 20.02; S, 9.17. Found: C, 47.96; H, 1.65; N, 19.92; S, 9.24.

2.2.1.2. 6-(4-Fluorobenzyl)-3-(pyridin-4-yl)-[1,2,4]triazolo[3,4-*b*][1,3,4]thiadiazole (4c)

Brown solid (75%): m.p 187-188 ^{o}C; R_f: 0.62 (10% MeOH/$CHCl_3$); IR (ATR, cm^{-1}): 3048 (Ar-H), 1602 (C=N), 1569, 1506 (C=C) 1218 (C-F); ^{1}H NMR (300 MHz, DMSO-d_6): δ 8.80 (bs, 2H, Ar-H), 8.14 (d, 2H, J = 5.7 Hz, Ar-H), 7.54-7.49 (m, 2H, Ar-H), 7.27-7.20 (m, 2H, Ar-H), 4.55 (s, 2H, CH_2); ^{13}C NMR (75 MHz, DMSO-d_6): δ 171.86, 163.74, 160.51, 156.42, 151.16, 143.72, 132.87, 131.99, 131.94, 131.87, 131.76, 119.83, 116.36, 116.07, 36.74. Analysis Calcd. for $C_{15}H_{10}FN_5S$: C, 57.87; H, 3.24; N, 22.49; S, 11.30. Found: C, 57.68; H, 3.32; N, 22.31; S, 11.43.

2.2.1.3. 3-(Pyridin-4-yl)-6-(*p*-tolyloxymethyl)-[1,2,4]triazolo[3,4-*b*][1,3,4]thiadiazolezole (4e)

Brown solid (78%): m.p 194-195 ^{o}C; R_f: 0.61 (10% MeOH/$CHCl_3$); IR (ATR, cm^{-1}): 3041 (Ar-H), 1605 (C=N), 1546, 1528 (C=C); ^{1}H NMR (300 MHz, DMSO-d_6): δ 8.82 (d, 2H, J = 6.0 Hz, Ar-H), 8.15-8.13 (m, 2H, Ar-H), 7.15 (d, 2H, J = 8.4 Hz, Ar-H), 7.03 (d, 2H, J = 8.7 Hz, Ar-H), 5.61 (s, 2H, OCH_2), 2.25 (s, 3H, CH_3); ^{13}C NMR (75 MHz, DMSO-d_6): δ 169.79, 156.02, 155.42, 151.21, 143.88, 132.77, 131.53, 130.55, 119.83, 115.46, 65.43, 20.55. Analysis Calcd for $C_{16}H_{13}N_5OS$: C, 59.43; H, 4.05; N, 21.66; S, 9.92. Found: C, 59.56; H, 3.96; N, 21.58; S, 9.74.

2.3. Single crystal Growth

The compounds **4a-e** were dissolved in hot solution of ethanol. On slow evaporation of the solvent at room temperature (20–25 °C), good quality crystals suitable for X-ray diffraction were obtained.

2.4. Single crystal data collection and structure solution

The X-ray measurements for all compounds were carried out on a Bruker APEXII Kappa CCD single crystal diffractometer equipped with a graphite monochromator. MoK_α radiation (λ = 0.71073 Å) was used for the collection, which was controlled by APEX2[53] with data collected at 90(2)K. Data were corrected for Lorentz and polarization effects using SAINT[53] and multi-scan absorption corrections were applied using SADABS[53]. The structures were solved by direct methods using SHELXS-97[54] and refined using full-matrix least-squares procedures with SHELXL-2014[55] and Titan2000[56]. All non-hydrogen atoms were refined anisotropically and all hydrogen atoms bound to carbon were placed in the calculated positions, and their thermal parameters were refined isotropically with U_{eq} = 1.2—1.5 U_{eq}(C). The molecular plots and packing diagrams were drawn using Mercury[57] and additional metrical data were calculated using PLATON[58].

2.4.1. Modelling of disorder

The *para*-methylphenoxy group and the pyridyl group in **4e** was observed to be disordered over two orientations, with occupancy ratios 0.428(9):0.572(9) and 0.434(8): 0.566(8) respectively. The disorder associated with this molecule was carefully modeled using the PART command in SHELXL2014[55]. The thermal parameters were constrained to be equal using the EADP command. The pyridine and benzene rings of both the major (labelled as "B") and the minor components were constrained to be a regular hexagon using the FLAT command with C−C bond lengths and C-C-C bond angles restrained using DFIX.

2.5. Theoretical calculations

2.5.1. Calculation of the Lattice energies and the Interaction Energies (I.E.)

Lattice energies of all the compounds were calculated by the PIXEL method in the CLP computer program package [version 12.5.2014] [59]. For this purpose all hydrogen atoms were moved to their corresponding neutron distances and accurate electron density around the molecule was calculated at MP2/6-31G** using Gaussian 09[60]. The total lattice energy was partitioned into their Coulombic, polarization, dispersion and repulsion contributions (**Table 2**). PIXEL energy calculations also provide molecule interaction energies (I.E.) related by the symmetry element in the crystal. The selected molecular pairs along with their interaction

energies (again with the total interaction energy partitioned into their Coulombic, polarization, dispersion and repulsion contributions) are presented in **Table 3**. The intermolecular interactions involved in linking molecular pairs also appear in **Table 3**. It was found that the results obtained by these PIXEL energy calculations are comparable to those calculated using high level MP2 and DFT-D quantum mechanical calculations[61].

2.5.2. Hirshfeld surface, 2D-Fingerprint plot and 3D deformation density

Hirshfeld surfaces mapped with different properties and 2D-fingerprint plots were generated using CrystalExplorer 3.0[62]. These have proven to be a useful visualization tool for the analysis of intermolecular interactions in the crystal packing[63]. The Hirshfeld surface is defined in a crystal as the region around a molecule where the ratio of the electron distribution of a sum of spherical atoms for the molecule (the *promolecule*) to the corresponding sum over the crystal (the *procrystal*) equals to 0.5. The shape and nature of the surface is directly influenced by the environment around the molecule in the crystal. The 2D-fingerprint plot provides quantitative information about the decomposition of the Hirshfeld surfaces into contributions from the different intermolecular interactions present in the crystal structure. In this study, the electrostatic potential (ESP) were mapped on the Hirshfeld surface[64] over the range -0.06 au (red), through 0 (white), to 0.06 au (blue). For this purpose, *ab initio* wavefunctions were obtained at HF/6-311G** using the Gaussian software. Molecular geometries were taken directly from the relevant crystal structure with H-atoms at their neutron distances. Further, 3D deformation density for the molecule at the crystal geometry has also been plotted over the electron density iso-surface (the value is 0.008 e/au^3) using CrystalExplorer 3.0. For this purpose, *ab initio* wavefunctions were also obtained at HF/6-311G**.

2.5.3. Calculation of Topological Parameters

Theoretical calculations based on the quantum theory of atoms in molecules (QTAIM)[65-66] were performed using the software AIMALL[67] on selected molecular motifs, extracted from the crystal structure. For this purpose, *ab initio* calculations for the selected dimers, were performed at the MP2/6-31G** level of theory using Gaussian 09. H-atoms were moved to their neutron distances before the calculation. Selected topological parameters including electron densities (ρ_b) and Laplacian operators ($\nabla^2\rho_c$) at the bond critical points (BCPs) were obtained (**Table 4**). The

local stabilization energy for the different intermolecular interactions was also estimated (**Table 4**) through an Espinosa−Molins−Lecomte (EML) relationship[68] as follows:

I. E. = $0.5V_b$ (in atomic units); where V_b is local potential energy density at the BCP.

Table 1: Crystallographic and Refinement Data

	4a	**4b**	**4c**	**4d**	**4e**
Empirical formula	$C_{11}H_6N_4O_2S$	$C_{14}H_6ClF_2N_5S$	$C_{15}H_{10}FN_5S$	$C_{14}H_9FN_4OS$	$C_{16}H_{13}N_5OS$
CCDC No.	1431641	1431642	1431643	990263	1431645
Formula weight	258.3	349.75	311.34	300.31	323.37
Temperature	90(2) K	90(2) K	90(2) K	90(2) K	90(2) K
Wavelength	0.71073 Å	0.71073 Å	0.71073 Å	0.71073 Å	0.71073 Å
Crystal system	Monoclinic	Tetragonal	Triclinic	Orthorhombic	Monoclinic
Space group	$P2_1/n$	$I4/m$	P-1	$Pbcn$	$P2_1/c$
Unit cell dimensions	a = 10.7264(7) Å, b = 4.9865(3) Å, c = 19.6574(13) Å, β = 92.788(4)°	a = 20.944(3) Å, b = 20.944(3) Å, c = 6.5748(9) Å, $\alpha = \beta = \gamma$ = 90°	a = 4.8756(4) Å, b = 10.3551(9) Å, c=13.4098(12) Å, α = 90.293(4)° β = 98.760(4)° γ = 90.571(4)°	a = 13.699(3) Å, b = 9.328(2) Å, c = 20.497(4) Å, $\alpha = \beta = \gamma$ = 90°	a = 11.3550(8) Å, b = 8.6409(7) Å, c = 15.7538(13) Å, β = 105.418(4)°
Volume	1050.17(12) $Å^3$	2884.0(9) $Å^3$	669.08(10) $Å^3$	2619.3(10) $Å^3$	1490.1(2) $Å^3$
Z	4	8	2	8	4
Density (calculated)	1.633 g cm^{-3}	1.611 g cm^{-3}	1.545 g cm^{-3}	1.523 g cm^{-3}	1.441 g cm^{-3}
Absorption coefficient	0.307 mm^{-1}	0.437 mm^{-1}	0.257 mm^{-1}	0.263 mm^{-1}	0.229 mm^{-1}
F(000)	528	1408	320	1232	672
Crystal size	0.50 × 0.21 × 0.05 mm^3			0.470 × 0.450 × 0.190 mm^3	
Theta range for data collection	3.804 to 33.336°	2.751 to 27.153°	1.967 to 34.104	2.482 to 26.307°	2.482 to 24.948°
Index ranges	-16<=h<=15; -7<=k<=7; -29<=l<=27	-15 =< h =< 16; 0 =< k =< 25; 0 =< l =< 8	-7 =< h =< 7; -15 =< k =< 16; -21 =< l =< 19	-17<=h<=14; -11<=k<=11; -25<=l<=25	-13<=h<=13; -10<=k<=10; -16<=l<=18
Reflections collected	18398	1439	15447	28565	16051
Independent reflections	3792 [*R*int = 0.0608]	1439 [*R*int = 0.0378]	4652 [*R*int = 0.0349]	2639 [R(int) = 0.0685]	2591 [R(int) = 0.0531]

Refinement method	Full-matrix least-squares on F^2	Full-matrix least-squares on F^2	Full-matrix least-squares on F^2	Full-matrix least-squares on F^2	Full-matrix least-squares on F^2
Data / restraints / parameters	3792/ 0 / 162	1439/ 0/ 139	4652/ 0/ 199	2639 / 0 / 190	2591/ 0/ 266
Goodness-of-fit on F^2	1.019	1.164	1.066	1.022	1.082
Final R indices [I>2sigma(I)]	R_1 = 0.0437, wR_2 = 0.1168	R_1 = 0.0722, wR_2 = 0.1848	R_1 = 0.0382, wR_2 = 0.0960	R_1 = 0.0352, wR_2 = 0.0900	R_1 = 0.0418, wR_2 = 0.1049
R indices (all data)	R_1 = 0.0695, wR_2 = 0.1313	R_1 = 0.0809, wR_2 = 0.1891	R_1 = 0.0480, wR_2 = 0.1021	R_1 = 0.0464, wR_2 = 0.0969	R_1 = 0.0576, wR_2 = 0.1146
Largest diff. peak and hole	0.522 and -0.376 eÅ^{-3}	0.632 and -0.722 eÅ^{-3}	0.504 and -0.255 eÅ^{-3}	0.225 and -0.309 eÅ^{-3}	0.220 and -0.267 eÅ^{-3}

Table 2: Lattice energy (kJ/mol) partitioned into Coulombic, polarization, dispersion and repulsion contributions by the PIXEL method.

	Code	E_{Coul}	E_{Pol}	E_{Disp}	E_{Rep}	E_{Tot}
1.	**4a**	-90.8	-37.2	-164.6	162.3	-130.3
2.	**4b**	-79.7	-33.4	-188.7	154.0	-147.8
3.	**4c**	-94.7	-41.6	-199.9	183.5	-152.6
4.	**4d**	-71.2	-26.9	-163.3	116.8	-144.6
5.	**4e**	-102.5	-46.3	-214.7	215.2	-148.4

Table 3: Interaction energies (I.E. in kJ/mol) obtained from PIXEL method for the different molecular pairs and the possible interactions involved. Neutron values are given for all D-H···A interactions.

Motifs	Symmetry code	Centroid-Centroid Distance (Å)	E_{Coul}	E_{Pol}	E_{Disp}	E_{Rep}	E_{Tot}	Selected Involved Interactions	Geometry (Å/ °)
4a ($P2_1/n$, Z = 4)									
I	**-x+1, -y+1, -z+1**	7.493	-72.8	-30.6	-30.8	102.7	-31.5	**S1···N2**	2.805(2)
II	**-x+1, -y, -z+1**	6.041	-15.1	-8.1	-28.7	21.3	-30.6	**Molecular Stacking Cg2···Cg2**	3.473(2)
III	**-x, -y-1, -z+1**	7.545	-8.3	-5.1	-32.0	22.4	-22.9	**C6-H6···O2**	3.386(2)/ 2.56/ 133
IV	**x-1/2, -y+1/2, z-1/2**	11.141	-20.8	-6.7	-10.2	15.4	-22.3	**C10-H10···N1**	3.252(2)/ 2.37/ 138
V	**-x, -y, -z+1**	5.182	-7.6	-3.1	-37.6	26.1	-22.2	**Molecular stacking Cg1···Cg4**	3.760(2)
VI	**x, y-1, z**	4.987	0.2	-5.8	-47.0	32.8	-19.7	**Molecular stacking Cg1···Cg2**	3.399(2)
VII	**-x+1/2, y+1/2, -z+1/2**	8.675	-8.0	-5.9	-25.4	22.7	-16.5	**C9-H9···Cg4**	3.525(2)/ 2.70/ 133
VIII	**x-1/2, -y-1/2, z-1/2**	11.372	-7.0	-2.4	-7.1	4.8	-11.6	**C11-H11···O1**	3.559(2)/ 2.49/ 171
4b ($I4/m$, Z = 8; Z' = 0.5)									
I	**y+1/2, -x+1/2, z+1/2**	6.813	-16.3	-7.6	-53.0	41.7	-35.2	**Molecular stacking C1···C11 (Cg2···Cg4)**	3.316(2)
II	**y, -x+1, z**	9.948	-27.6	-11.8	-23.5	35.0	-27.8	**C11 -H11···N5**	3.240(2)/ 2.18/ 167

								C14 -H14···F1 C12-F1···F2-C13	3.457(2)/ 2.62/ 134 2.908(2)/ 143(1)/ 111(1)
III	-x+3/2, -y+1/2, z+1/2	7.889	-0.4	-1.8	-26.1	5.0	-23.4	Molecular stacking C5···C5 (Cg1···Cg1)	3.700(2)
IV	-x+1, -y, z	8.439	-21.5	-11.5	-29.7	43.1	-19.5	Cl1···N2 S1···S1	3.070(2) 3.431(2)
V	y+1, -x+1, z	13.107	-8.1	-3.6	-10.0	9.2	-12.5	C6 -H6···N2 C6 -H6···N1	3.600(2)/ 2.53/ 172 3.589(2)/ 2.68/ 141
4c (*P*-1, *Z* = 2)									
I	-x+2, -y+1, -z+1	5.664	-33.5	-13.7	-52.1	44.0	-55.2	C15-H15···N1 Molecular stacking C3···N2 (Cg2···Cg2)	3.603(2)/ 2.62/ 150 3.260(2)
II	-x+3, -y, -z+1	7.212	-35.4	-14.5	-51.7	51.6	-50.0	C7-H7···N4 C9-H9B···N5	3.556(2)/ 2.50/ 165 3.580(2)/ 2.65/ 144
III	x+-1, y, z	4.876	-7.6	-11.5	-69.6	52.8	-35.9	C9-H9A···C11 C1···C7 (Cg2···Cg1)	3.849(2)/ 2.77/ 172 3.315(2)
IV	-x+2, -y, -z+1	6.377	-10.9	-3.6	-30.0	10.8	-33.7	Molecular stacking C2···C7 (Cg3···Cg1)	 3.782(2)
V	-x+1, -y+1, -z+1	8.324	-74.3	-30.6	-32.0	108.8	-28.2	S1···N2	2.807(2)
VI	x, y, z-+1	13.410	-5.3	-1.4	-10.6	7.1	-10.3	C5 -H5···F1 C6 –H6···F1	3.168(2)/ 2.42/ 125 3.288(2)/ 2.65/ 117
4d (*Pbcn*, Z = 8)									
I	-x+1, -y, -z+1	5.914	-26.6	-11.5	-65.0	56.7	-46.4	C8-H8B···O1	3.410(2)/ 2.47/ 145
II	-x+1/2, y-1/2, z	5.988	-8.9	-7.2	-50.5	33.2	-33.4	C5-H5···C7 C8-H8A···C5 C10-H10···C1	3.738(2)/ 2.81/ 144 3.758(2)/ 2.68/ 174 3.666(2)/ 2.86/ 131
III	x, y+1, z	9.328	-16.1	-5.3	-17.6	13.1	-25.9	C8-H8B···O1 C14-H14···N1	3.386(2)/ 2.52/ 136 3.385(2)/ 2.59/ 130
IV	-x+1, -y-1, -z+1	12.367	-17.7	-6.8	-14.2	12.9	-25.9	C7-H7···N1	3.526(2)/ 2.66/ 137
V	x-1/2, y+1/2, -z+3/2	9.940	-12.3	-5.4	-11.5	13.8	-15.4	C11-H11···N2	3.382(3)/ 2.40/ 150
VI	x, -y, z-1/2	10.382	-3.6	-1.1	-10.3	5.9	-9.1	C7-H7···F1	3.223(2)/ 2.57/ 118
4e ($P2_1/c$, Z = 4)									
I	x, -y+1/2, z-1/2	8.021	-25.4	-11.0	-61.1	54.7	-42.8	C9-H9A···N1 C5B-H5B···S1 Molecular stacking C4B···C10B C1···C11B	3.425(2)/ 2.44/ 150 3.526(2)/ 2.76/ 127 3.319(2) 3.393(2)
II	-x+1, -y+1, -z+1	7.055	-27.1	-13.9	-82.5	85.1	-38.4	Molecular stacking Cg1···Cg3	3.431(2)
III	-x+1, -y, -z+1	8.715	-56.4	-22.0	-25.9	71.3	-33.0	S1···N2	2.913(2)
IV	x, -y+3/2, z+1/2	10.622	-16.8	-7.4	-20.9	21.7	-23.4	C11B-H11B···N5B C9-H9B···N5B	3.555(8)/ 2.48/ 172 3.451(5)/ 2.75/ 122
V	-x, y-1/2, -z+3/2	10.005	-8.3	-5.3	-31.9	25.5	-20.1	C15B-H15B···C12B	3.585(2)/ 2.71/ 138
VI	-x+1, y+1/2, -z+1/2	13.684	-8.1	-3.2	-9.0	7.4	-12.9	C6B-H6B···N1	3.551(7)/ 2.56/ 152

Table 4: Topological parameters for the selected interactions in different molecular motifs of **4a**, **4b** and **4c.**

Compound code_ motif	Interaction	Bond path [R_{ij} (Å)]	Electron density [ρ_{BCP} (e/Å^3)]	Laplacian [$\nabla^2\rho_{BCP}$ (e/Å^5)]	EML[35] Interaction energy (kJ/mol)
4a_I	**S1···N2**	2.809	0.137	1.469	18.4
	N2···N2	3.016	0.067	0.791	9.1
4b_II	**H11···N5**	2.197	0.134	1.476	15.6
	F1···F2	2.917	0.039	0.731	7.3
	H14···F1	2.655	0.032	0.484	4.5
4b_IV	**S1···Cl1 (intra)**	2.982	0.131	1.652	18.5
	Cl1···N2	3.083	0.074	0.921	9.5
	S1···S1	3.442	0.057	0.735	6.0
4c_V	**S1···N2**	2.816	0.136	1.474	18.5
	N2···N2	2.921	0.081	0.973	11.0

3. Results and Discussion

3.1. Chemistry

The reaction sequences employed for the synthesis of title compounds are illustrated in **Scheme 1**. The carbohydrazides **(1a-c)**, on reaction with carbon disulfide in methanolic potassium hydroxide afforded the corresponding dithiocarbazinates **(2a-c)** in good yields and were directly used for the next step without further purification. The corresponding 4-amino-1,2,4-triazole-3-thiols **(3a-c)** were then synthesized by refluxing salts **(2a-c)** with hydrazine hydrate (80%).

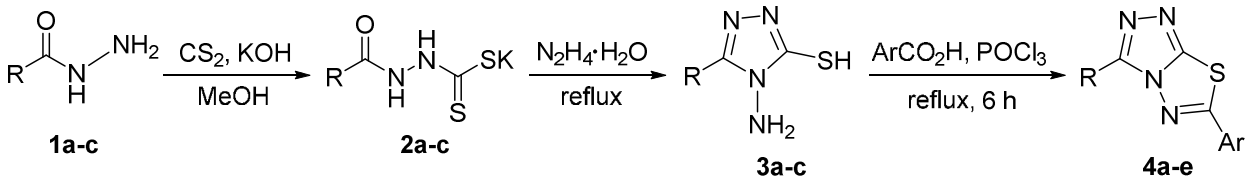

4a R = 2-furanyl **Ar** = 2-furanyl
4b R = 3-pyridyl **Ar** = 2-Cl,4,5-F_2-C_6H_2
4c R = 4-pyridyl **Ar** = 4-F-$C_6H_4CH_2$
4d R = 2-furanyl **Ar** = 4-F-C_6H_4-CH_2
4e R = 4-pyridyl **Ar** = 4-CH_3-C_6H_4-OCH_2

Scheme 1. Synthetic protocol for the preparation of triazolothiadiazoles **(4a-e)**.

Condensation of the appropriate triazole **(3a-c)** with various aromatic/hetero-aromatic carboxylic acids in phosphorous oxychloride under reflux provided access to a diverse array of 1,2,4-triazolo[3,4-*b*][1,3,4]thiadiazoles **(4a-e)** in good yields[48,50-51]. The appearance of new stretching bands in the IR spectra and disappearance of characteristic peaks for the –SH and $–NH_2$ groups clearly indicated the smooth cyclization. Signals observed at 4.55 and 5.61 ppm as singlets for the methylene group confirmed the formation of triazolothiadiazoles **(4c, e)**. ^{13}C NMR spectra of the condensed heterocycles showed the presence of carbon signals at appropriate chemical shift values. The purity of the newly synthesized hybrid compounds was also determined by elemental analysis.

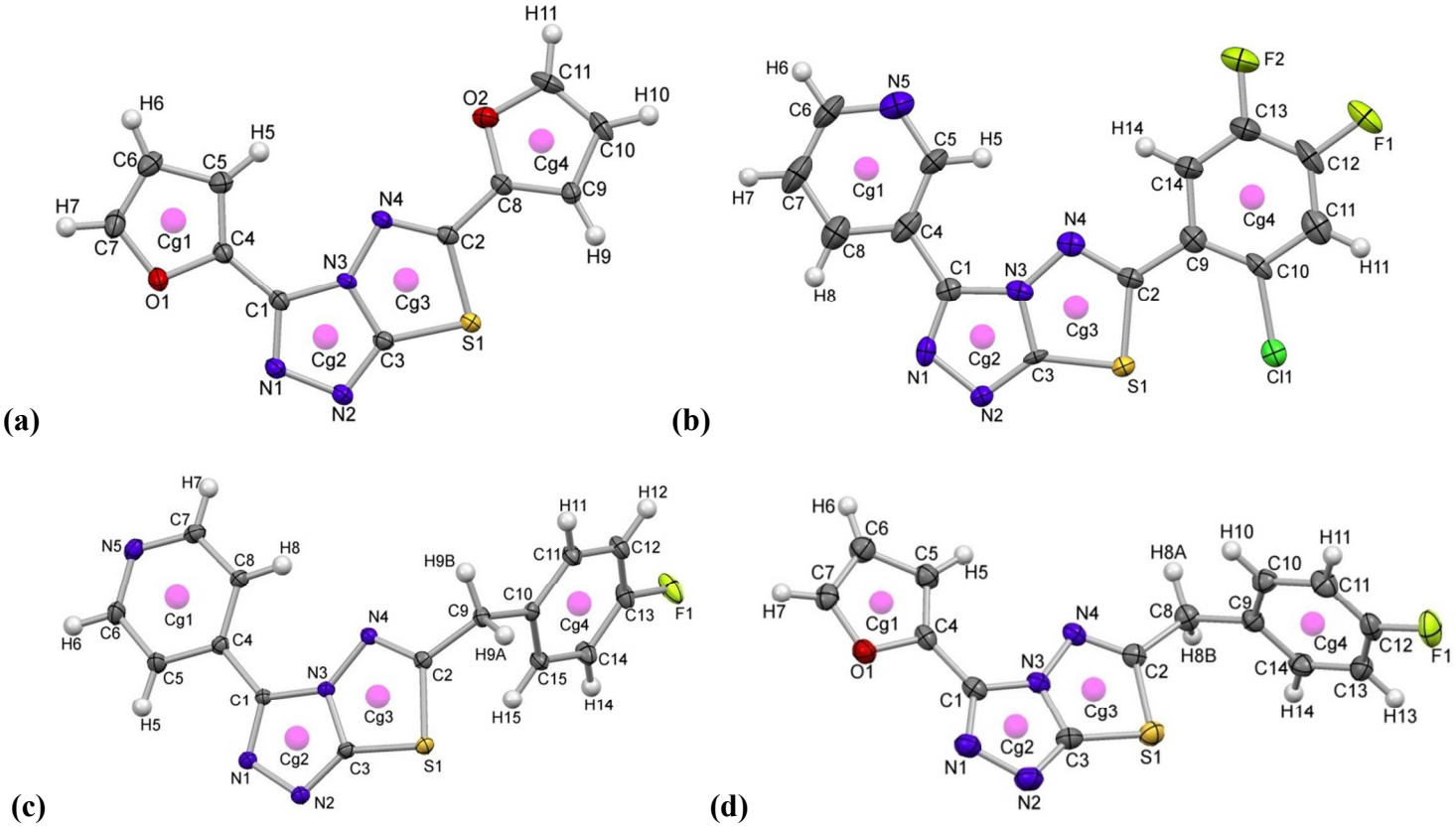

(e)

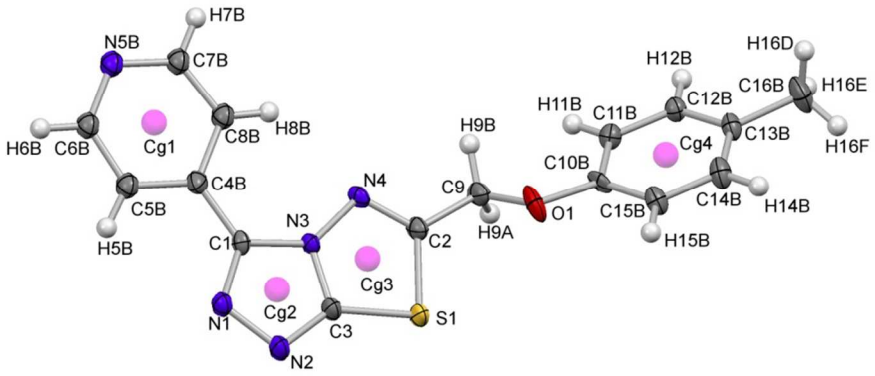

Figure 1: *ORTEP* plots of **(a) 4a (b) 4b (c) 4c (d) 4d** and **(e) 4e** showing the atom numbering, with ellipsoids drawn with 50% probability level. "Cg*n*" represents the centroid of the *n*th ring, shown by magenta spheres. For clarity only the major components of the disordered pyridyl and tolyl rings in **4e** are shown.

3.2. Molecular structures

The structures of the five reported molecules, **Fig. 1**, are sufficiently similar to be discussed together. Although the structure of **4d** has been reported previously[52] it is included in this discussion for comparative purposes. Each molecule comprises a central triazolothiadiazole unit with substitiuents on the C1 carbon atom of the triazole ring and the C2 carbon of the thiadiazole unit. 2-furanyl substituents are found on C1 and C2 for **4a** and on C1 for **4d**. In contrast C1 carries a 3-pyridyl substituent in **4b** and 4-pyridyl rings in **4c** and **4e**. Interestingly, all previously studied triazolothiadiazole compounds in the Cambridge Crystallographic Database[69] are characterized by the presence of substituents on the C atoms of both the triazolo- and thiadiazole rings as is found here. Compounds **4a** and **4b** with aromatic substituents at C1 and C2 are planar, **4b** strictly so, suggesting a reasonable degree of conjugation over the entire molecule. The benzyl substituents at C2 for **4c**, **4d** and **4e** destroy the molecular planarity although for **4c** and **4d** the C1 pyridyl substituents remain close to the plane of the triazolothiadiazole ring system. Despite the disorder in the pyridyl ring for **4e** both components also lie reasonably close to the triazolothiadiazole plane.

Bond distances and angles within the triazolothiadiazole unit compare reasonably well with those of 40 other triazolo[3,4-*b*][1,3,4]thiadiazole derivatives whose structures were found in the Cambridge Crystallographic database[69]. 11 additional structures are found in which triazolothiadiazole derivatives act as ligands to transition metal complexes, binding to the metal exclusively *via* the N2 atoms of the triazole rings[70-71]. A significant elongation of the S1—C2 distance in comparison to S1—C3 bond in the molecules reported here appears from comparison with related compounds to be a characteristic feature of triazolo[3,4-*b*][1,3,4]thiadiazoles. Only three instances of compounds with furan substituents have been reported previously, two with the furan on the triazole[50-52] and the other on the thiadiazole ring[72].

3.3. Crystal packing analysis: Inputs from PIXEL energy calculations

Lattice energy calculations, using the PIXEL method, for all compounds shows that the dispersion energy is the major component (56-62 %, **Table 2**), a well-known finding in the case of organic molecules. However, it was also observed that compounds **4a, 4c** and **4e** exhibit a significant electrostatic (coulombic + polarization, 128, 136.3 and 148.8 kJ/mol) and repulsion contributions (162.3 kJ/mol, 183.5 kJ/mol and 215.2 kJ/mol) for **4a, 4c** and **4e** respectively). This was not found to be the case for **4b** and **4d** (**Table 2**). The presence of different kinds of intermolecular interactions that are involved in the crystal packing of these molecules may explain this observation. This will be extensively analyzed in the following section *via* inputs from both experimental and theoretical procedures.

3.3.1. Analysis of the molecular packing in 4a

The compound **4a** crystallizes in the centrosymmetric monoclinic space group $P2_1/n$ with $Z = 4$. Two interactions, inversion dimer formation resulting from short S1…N2 contacts [labelled **I**, Figure **2(a)**] and an offset π···π stacking interactions involving adjacent triazole rings [labelled **II**, Figure **2(a)**] show the greatest stabilization, with I.E. = -31.5 kJ/mol for **I** and I.E. = -30.6 kJ/mol for **II**. The short inversion related S1···N2 contacts have $d_{S\cdots N}$ = 2.805(2) Å, which is 0.55Å shorter than the sum of the van der Waals radii[73] of sulfur (1.80 Å) and nitrogen (1.55 Å). Partition of the total stabilization energy into different energetic contributions shows a very high contribution from the repulsion component (102.7 kJ/mol) in comparison to those found for **4b** and **4d**, **Table 2**). An increase in the repulsion component for the shorter contacts, leading to the

formation of molecular pairs in a crystal with reduced stability, has been observed previously[74]. Furthermore, the electrostatic (Coulombic + polarization) contribution is 77% of the total stabilization energy for motif **I** in **4a** suggesting that the S···N contact in motif **I** is principally electrostatic in origin. The stabilization energy of this dimer is comparable to the previously reported interaction energy of a selenadiazole dimer[75].

In order to gain more insights into the nature of this short S…N contact for **4a**, it was also analyzed by considering the Hirshfeld surfaces and 2D-fingerprint plots. The electrostatic potential mapped on the Hirshfeld surface of **4a** displays the presence of a positive ESP on the S-atom (σ-hole) of magnitude +0.085au. This electropositive region on the S-atom interacts with an electronegative region over the N-atom (-0.093au) resulting in the formation of the short dimeric S···N contact in the crystal packing. Its contribution to the Hirshfeld surface of **4a** is 7.3% [**Fig. 2(b)**]. This observation confirms the electrostatic origin of such S···N interactions and may be classified as a "chalcogen bond"[20-25]. A pair of spikes for the S···N contacts was observed on the decomposed 2D-fingerprint plot.

3D-deformation density (DD) maps were also plotted using Crystal Explorer. The wave function was calculated at the HF/ 6-311G(d,p) level using Gaussian. This reveals the presence of a charge depletion (CD) region at the S1 which is directed towards the charge concentration (CC) region over N2, facilitating formation of the S1···N2 contacts in the crystal [**Fig. 2(c)**]. Theoretical calculations based on the quantum theory of atoms in molecules (QTAIM) using AIMALL confirms the presence of a bond critical point (BCP) for the S···N interaction (R_{ij} = 2.809 Å) **[Fig 2(d)]**. Values for the topological parameters at the BCP are $\rho_b = 0.137$ e/Å^3 for the electron density, and $\nabla^2\rho_b = +1.469$ e/Å^5 for the Laplacian, (**Table 4**). The presence of a BCP for an N2···N2 contact was also observed in the molecular pair with a longer bond path length (R_{ij} = 3.016 Å). The short dimeric S1···N2 contacts clearly impose this relatively close approach of the N2 atoms. As a consequence of this, the CC regions on the two N2 atoms approach close to one another, as seen in the 3D-deformation density (DD) map [**Fig. 2(c)**]. This may explain the high repulsion energy contribution towards this molecular motif **I, Fig 2a**. However, in the crystal packing of **4a** the interactions between the CD and CC regions in the S1…N2 contact provides the overall stabilization in this motif.

A second stabilizing contact with similar stabilization energy (motif **II**, -30.6 kJ/mol, *d* = 3.4737(9) Å) results from an offset π···π interactions, involving adjacent triazole rings [centroid 'Cg2', **Fig. 2(b)**] with a contribution from the dispersion energy of 55%. Interestingly, this value is significantly less than the dispersion energies found for other π···π contacts formed by these molecules [motifs **V**, Cg1···Cg4, *d* = 3.7601(10) Å and **VI**, Cg1···Cg2, d = 3.3988(9) Å, **Table 3**)] where the contributions from the dispersion energies are 78% and 89% for motifs **V** and **VI** respectively.

Molecular packing in **4a** involves the formation of a chain of molecules approximately along the crystallographic *a*- axis through the S1···N2 inversion dimers, **I**, together with C6—H6···O2 hydrogen bonds (motif **III**, I.E. = -22.9 kJ/mol) [**Fig. 2(a)**]. The C—H···O hydrogen bonds generate $R^2_2(20)$ rings[76]. Both sides of these chains are bordered by another set of molecules that lie almost at right angles to the chain. These are linked to molecules in the chain by C10—H10···N1 (motif **IV**, I.E. = -22.3 kJ/mol), C9—H9···Cg4 (motif **VII**, I.E. = -16.5 kJ/mol) and C11—H11···O1 (motif **VIII**, I.E. = -11.6 kJ/mol) hydrogen bonds These bordering molecules are also stacked as a result of the **II**, **V** and **VI** π···π stacking interactions, as mentioned previously [**Fig. 2(a)**].

The electrostatic potential has been mapped over the Hirshfeld surface of **4a** [**Fig. 2(f)**]. A clear separation of the electropositive and electronegative regions was observed over the flat surfaces of the planar **4a** molecule. An electronegative region is found on both the faces of the molecule in the vicinity of the O1 furan ring centroid, Cg1 and for half of the triazole ring, Cg2. The other half of the triazole ring, the thiadiazole and the O2 furan rings lay in an area of positive potential. These observations support the observation of π···π stacking interactions with motifs **II**, **V** and **VI**. It is interesting to note that the two furan rings each have opposite potentials on both faces of the molecule which clearly facilitates the π···π (Cg1···Cg4) contact between them.

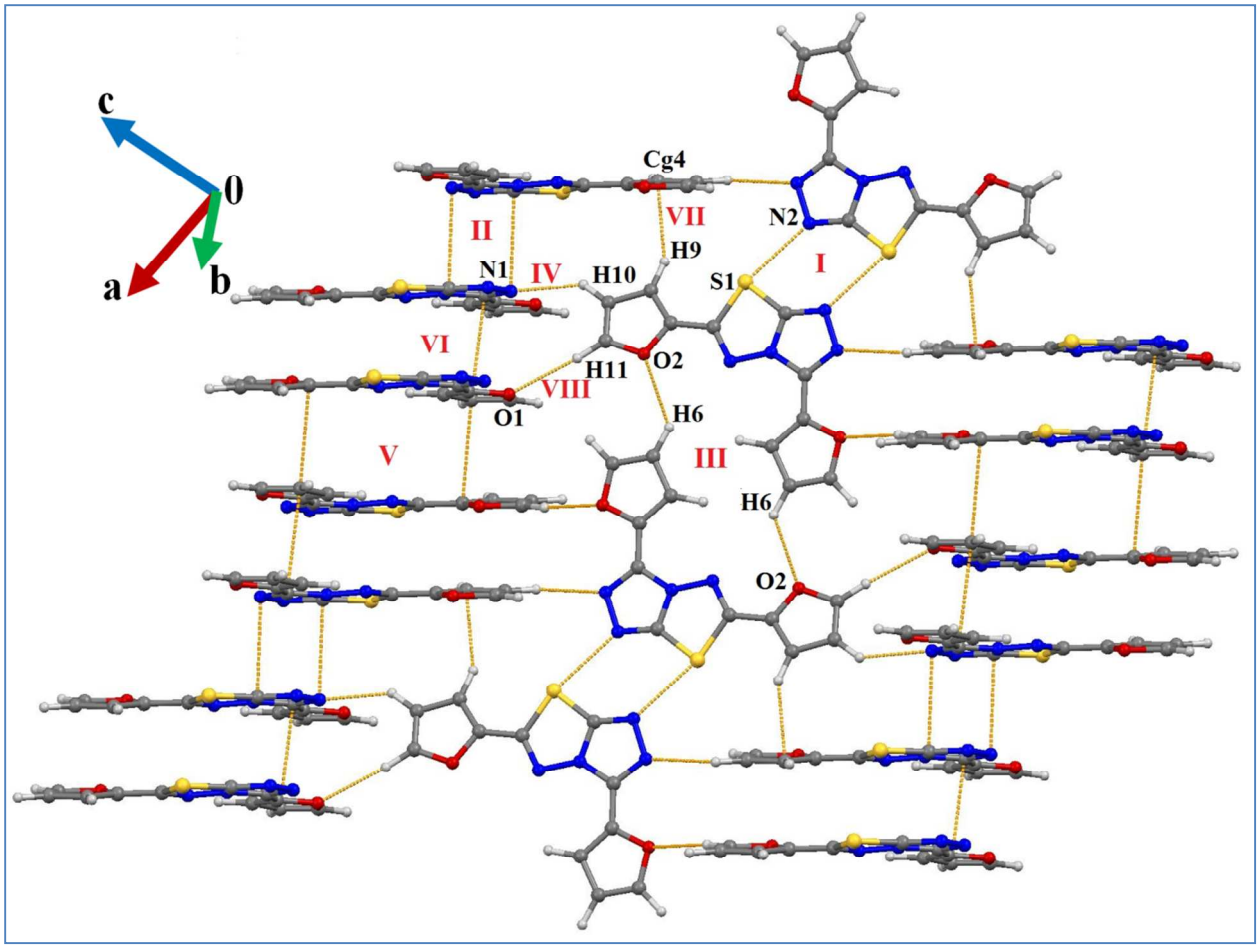

Figure 2(a): Packing of molecules in **4a** stabilised by dimeric S···N chalcogen bonds, π···π interactions and weak C-H···O and C-H···N hydrogen bonds. Roman numerals (in red) in this and subsequent diagrams indicate the molecular motifs detailed in **Table 3**.

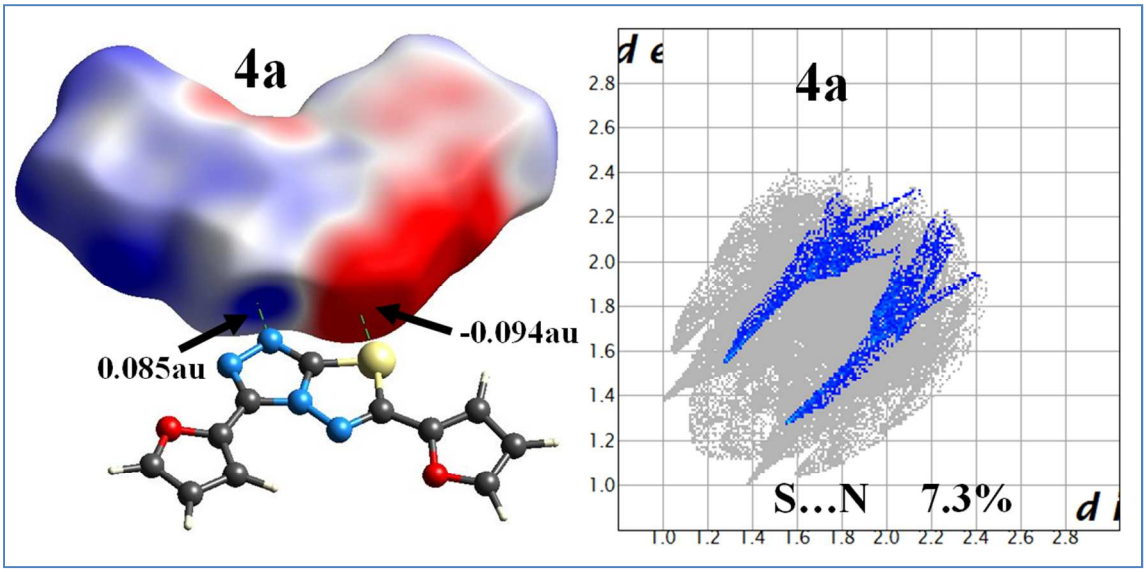

Figure 2(b): The Hirshfeld surface for **4a** mapped with electrostatic potential (**ESP**) over the range -0.06 au (red) through 0.0 (white) to 0.06 au (blue) for **4a**. The corresponding decomposed 2D fingerprint plot for the S···N contact is also presented.

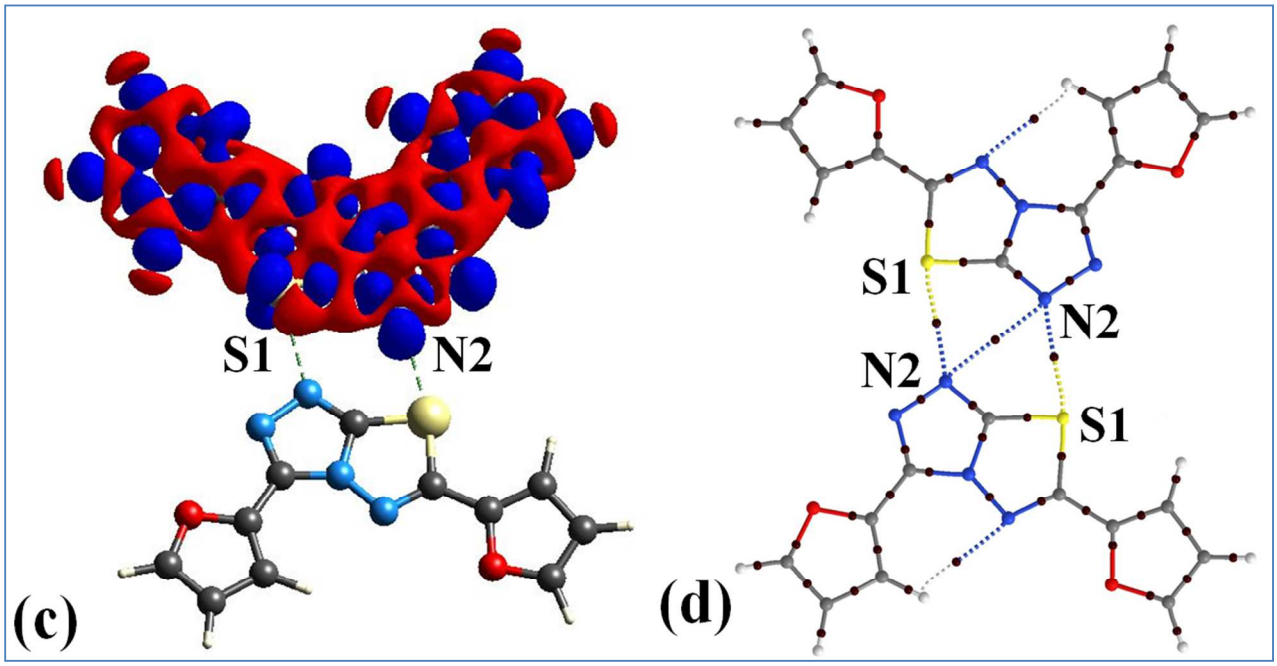

Figure 2(c): 3D-deformation density map for **4a** showing the presence of CD regions (in red) and CC regions (in blue), mapped using Crystal Explorer 3.0. The isosurfaces are drawn at 0.008 eau^{-3}. **(d)** A molecular plot of a selected dimer, showing the presence of bond critical points (brown spheres) for the various intermolecular contacts (**Table 4**).

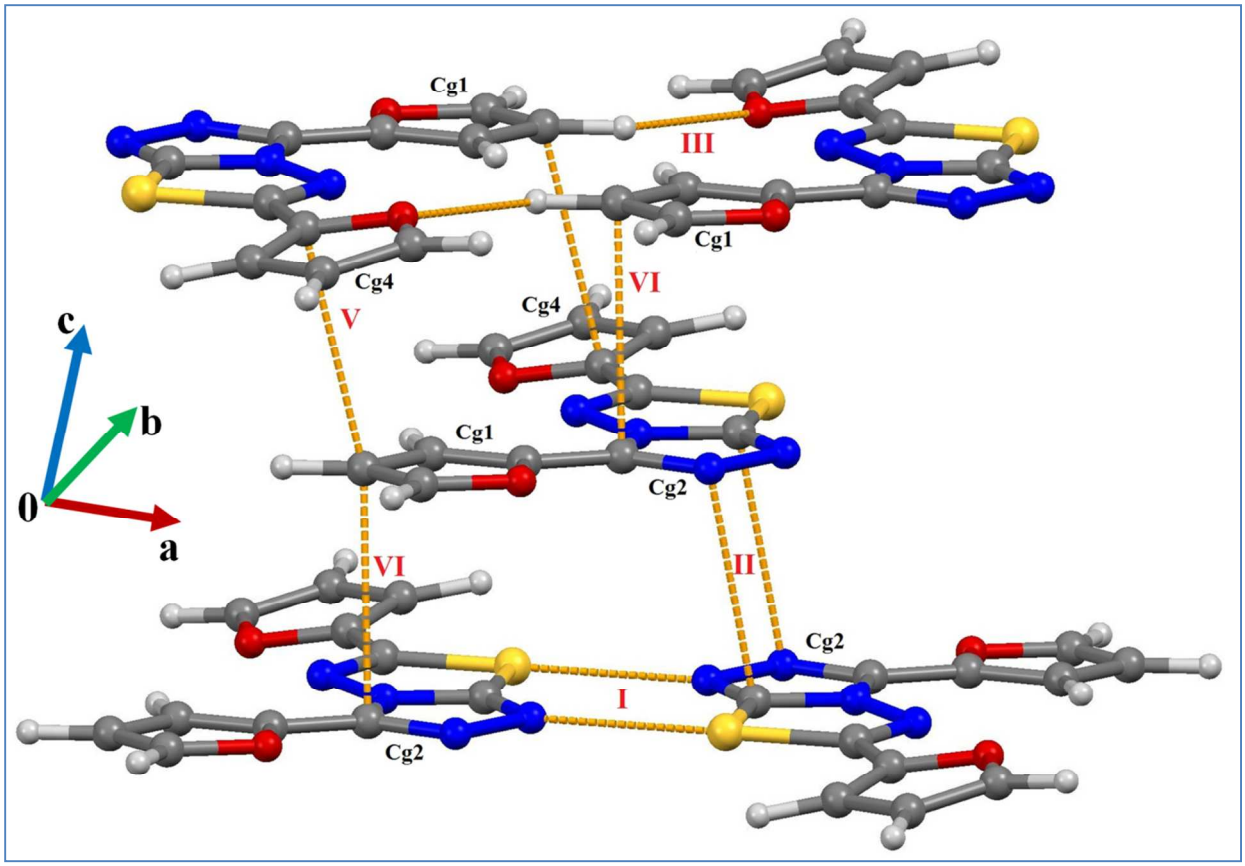

Figure 2(e): Packing of molecules in **4a**, displaying the different molecular layers, formed by S···N chalcogen bonds and weak C-H···O hydrogen bonds both of which form inversion dimers. The layers are interconnected by π···π stacking interactions.

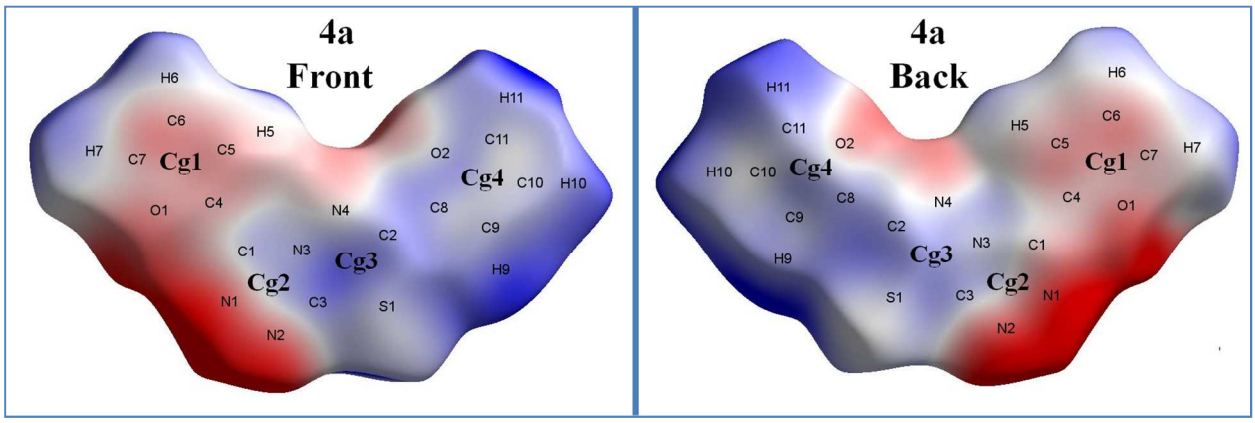

Figure 2(f): Front and back view of the electrostatic potential (**ESP**) mapped over the Hirshfeld surface for **4a** in the range -0.06 au (red) through 0.0 (white) to 0.06 au (blue).

3.3.2. Analysis of the molecular packing in 4b

The compound **4b** crystallizes in the centrosymmetric tetragonal *I*4/*m* space group with Z = 8. The entire molecule was observed to lie on a mirror plane parallel with the crystallographic *ab* plane, with one half of the molecule (Z' = 0.5) in the asymmetric unit.

Unlike **4a,** with two furan substituents on the triazolothiadiazole ring system, **4b** has a pyridine ring bound to C1 of the triazole ring and a difluorochlorobenzene substituent on C2 of the thiadiazole ring. With all atoms lying in the mirror plane the molecule is strictly planar which facilitates π-stacking interactions in the crystal packing. Indeed the most stabilized dimeric molecular pair (motif **I**, IE = -35.2 kJ/mol, *d* = 3.316Å) was observed to consist of π···π interactions, involving the triazole ring [labeled with 'Cg2', **Fig. 3(a)**] with the difluorochlorobenzene ring (Cg4), the contribution from dispersion energy being 52%.

Electrostatic potentials mapped over the Hirshfeld surface of **4b** reveal a flat smooth surface with similar characteristics to those previously observed for **4a**. Cg1 and half of the Cg2 ring have electronegative surfaces on both faces while the remainder of the surface, covering Cg3 and Cg4, is electropositive [**Fig. 3(b)**]. Hence the triazole and difluorochlorobenzene rings exhibit opposite electrostatic complementarity leading to significantly strong π···π stacking in the crystal packing. This is commensurate with motif **I** being the most stabilized contact in **4b** [**Figs. 3(a)** & **3(b)**]. This is the only interaction observed for this molecular pair which has a 32% electrostatic contribution towards the total interaction energy (**Table 3**). This is a "*very rare supramolecular feature*" as π···π interactions are primarily considered to be dispersive in origin[77]**.**

An additional heavily offset π···π stacking interaction **III** (IE = -23.4 kJ/mol) results from an interaction between adjacent pyridine rings that lie in the electronegative regions of the Hirshfeld surface. Despite the substantial offset, C5 atoms on adjacent rings are separated by 3.700(2) Å. In sharp contrast to **I** where electrostatic effects play a significant role, this motif is found to have a 92% contribution from the dispersion energy, **Table 3**.

In addition to these π···π stacking interactions, an eclectic mix of intermolecular C—H…N and C—H···F hydrogen bonds, Cl1···N2 [3.071(6) Å], type II F1···F2, halogen bonds and short S1···S1 contacts, 3.432(3) Å, link each molecule to four others and generate infinite, strictly

planar sheets in the *ab* plane [**Fig. 3(c)**]. The second most stable molecular pairing motif **II**, (IE = -7.8 kJ/mol) results from a short, directional C11—H11···N5 hydrogen bond, bolstered by a C14—H14···F1 hydrogen bond, involving the highly acidic atom H14, and an F···F halogen bond, 2.908(8) Å, that approximates to type II geometry[78-79]. The strength of the C—H···N contact can be attributed to the acidity of the H11 atom that lies between two F atoms and a Cl atom and the well-recognized basicity of the pyridine N atom. The PIXEL calculations show that the total contribution from electrostatic effects is extremely high and found to be 63% for motif **II** (**Table 3**). The 3D deformation density map for the motif **II** [**Fig. 3(d)**] clearly shows that H11 points towards the CC region around the pyridine nitrogen atom, N5. Moreover, for the F···F halogen bond, the map shows clearly that the CD region of F1 points towards the CC region on F2[80]. Topological calculations based on QTAIM theory on a dimer generated by motif **II** confirms the presence of a (3, -1) BCP for the C—H···N, F···F and C—H···F interactions [**Figs. 3(e), Table 4**].

The electronic nature of the motif **II** was further analyzed from the ESP mapped over the Hirshfeld surface for **4b**. In the C11—H11···N5 contact, the highly electropositive region (0.112 au) around H11 interacts with highly electronegative (-0.100 au) region around the N5 [**Figs. 3(f)**]. This also confirms the strongly electropositive character of H11 and correspondingly strong electronegative nature of N5 as discussed previously. The pair of sharp spikes observed on 2D-fingerprint plot for this contact, is characteristic of a strong interaction. These observations also reflect the substantial electrostatic component found for this motif in the PIXEL calculations.

An obvious feature of the sheets of **4b** molecules formed in the *ab* plane are the inversion dimers generated by pairs of Cl1···N2 halogen bonds together with an S···S chalcogen bond (motif **IV**, IE = -19.5 kJ/mol). There are some similarities between this motif and the inversion related S···N contacts adopted in motif **I** by **4a**, consisting of dimeric S···N contacts. A significant difference between the two motifs is that for **4b** the molecules are translated away from one another to accommodate the longer N1···Cl1 and S1···S1 distances. An immediate effect of this translation is that sensible S···N contacts are precluded. The presence of two fluorine substituents on the benzene ring makes the Cl-atom more electron-deficient and polarizes the electron density with a larger CD region on the Cl-atom opposite to the C-Cl bond [**Fig. 3(d)**]. This facilitates

attraction by the CC region about N2 forming the two Cl···N halogen bonds[81]. The deformation map also shows some polarization of the electron density around the S-atom such that it is not directed towards the N2 atom. Instead, the intermolecular S···S chalcogen bond forms with equivalent C3—S1···S1 angles, and is reminiscent of the well-known situation[82] with *type I* halogen bonds. However, the CD region about the S atom does face the CC region on the adjacent Cl1 atom facilitating the formation of an intramolecular S···Cl chalcogen bond[83] [**Fig. 3(d)**].

QTAIM calculations on a dimer generated by motif **IV** again shows the presence of (3, -1) BCP's [**Fig. 3(e)**] and provides additional evidence about the formation of these contacts in the crystal packing of **4b** (**Table 4**). Furthermore, the Hirshfeld surface shows electropositive region (σ-hole, +0.056 au) on the Cl1 ideally positioned to interact with the highly electronegative region over N2 (-0.094 au) resulting in the formation of the halogen bond [**Fig. 3(g)**]. The ESP over S1 is moderately positive but the value is much less in comparison to the value found for **4a** leading to the formation of the S···N chalcogen bond. A pair of spikes was observed in the decomposed 2D fingerprint plots for the Cl···N interaction with the S···S contact generating a single spike. No characteristic signature was observed for the S···N contact as expected [**Fig. 3(g)**].

The final items in the extensive catalogue of contacts stabilizing the packing of **4b** are a pair of weak bifurcated C6—H6···N1 and C6—H6···N2 hydrogen bonds [motif **V**, IE = -12.5 kJ/mol] **Figure 3(c)**. The latter is short, highly directional and close to linearity (2.53Å, 172°) while the other is a weaker contact (2.68 Å, 141°), **Table 3**.

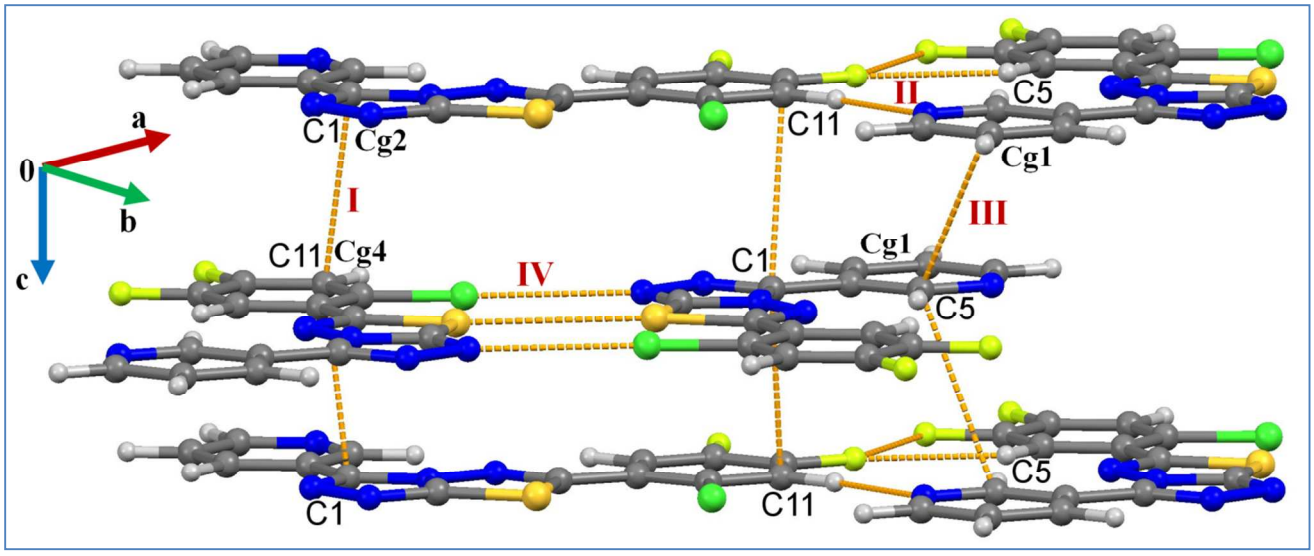

Figure 3(a): Formation of layers of **4b** molecules along the *c* axis through π···π interactions.

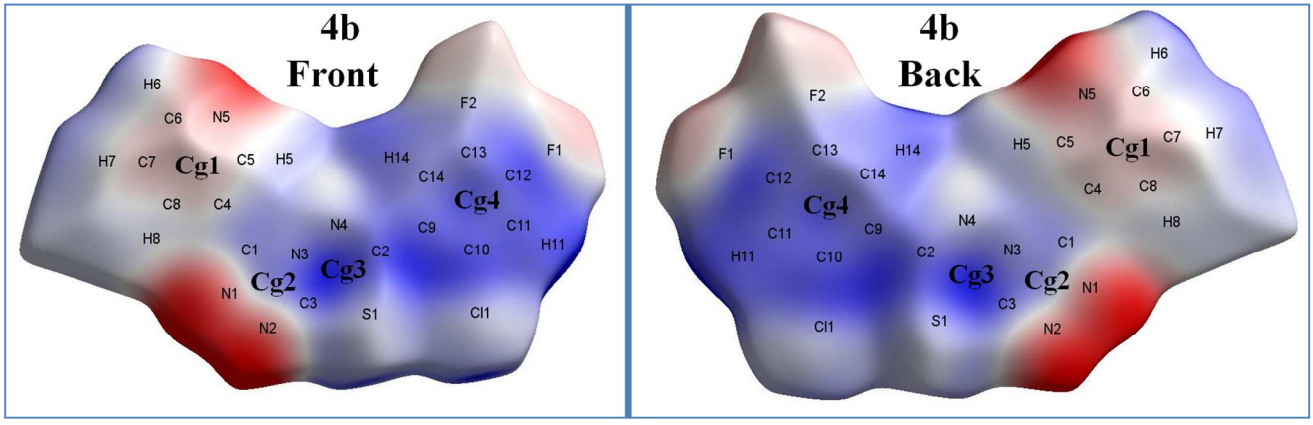

Figure 3 (b): Front and back view of the electrostatic potential (**ESP**) mapped over the Hirshfeld surface for **4b** over the range -0.06 au (red) through 0.0 (white) to 0.06 au (blue).

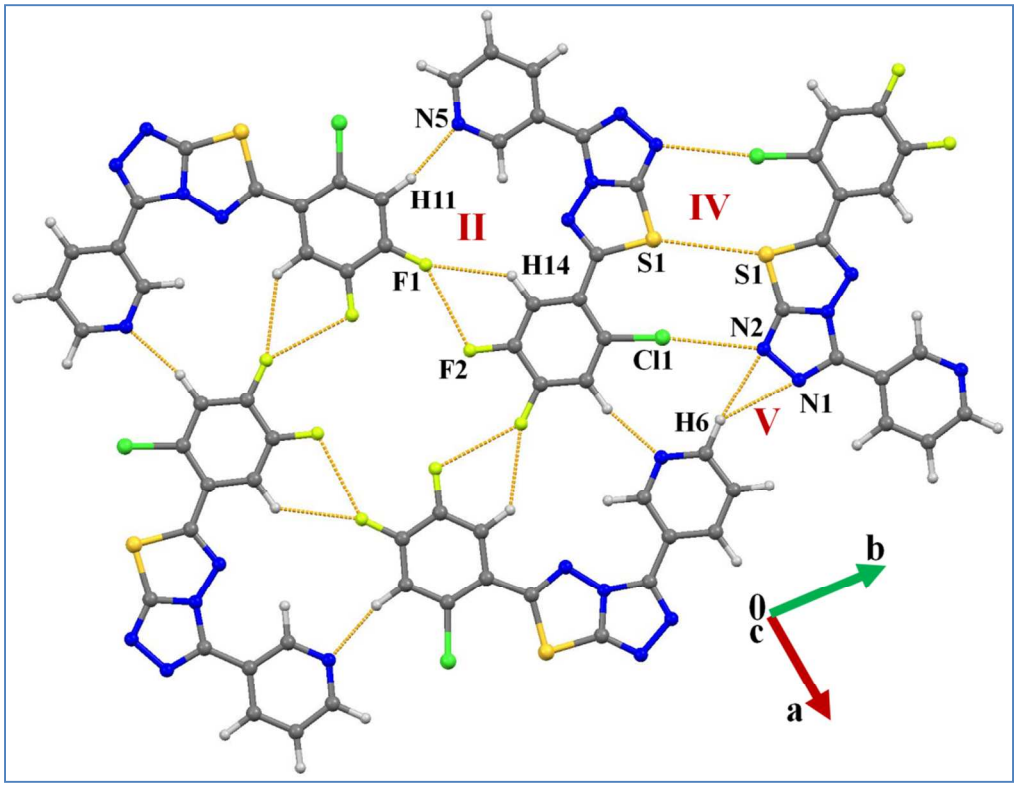

Figure 3(c): Packing view perpendicular to the *ab* plane for **4b** showing the formation of a molecular sheet due to Cl···N, S···S and F···F contacts together with weak C-H···N and C-H···F hydrogen bonds.

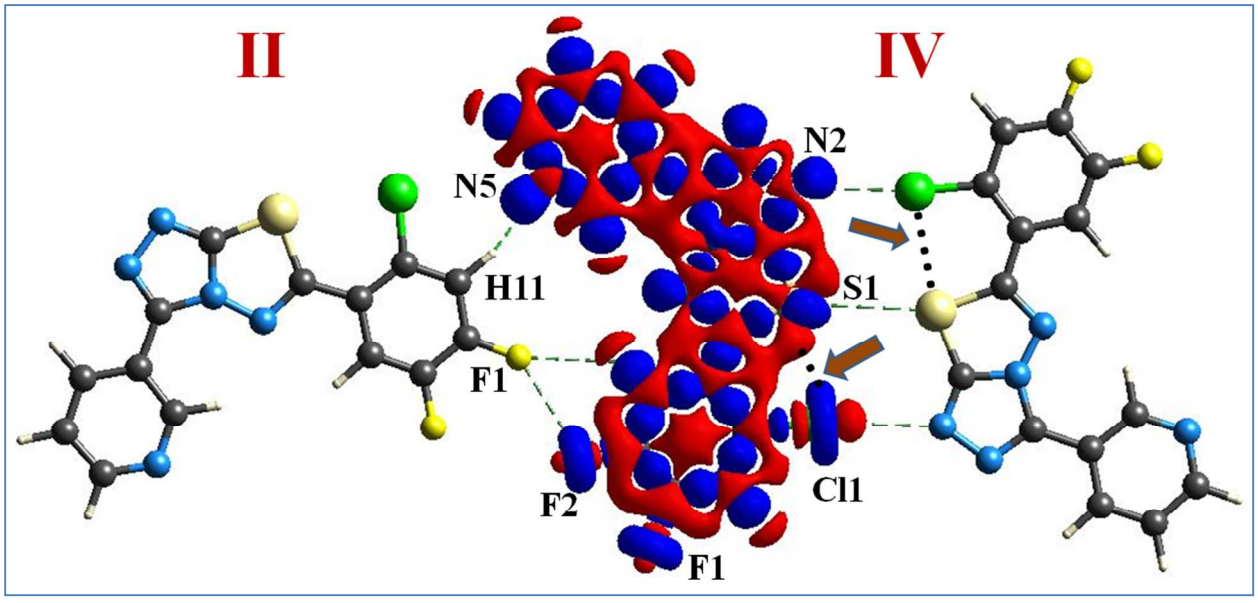

Figure 3(d): A 3D-deformation density map showing the presence of CD regions (in red) and CC regions (in blue) on the **4b**, mapped by Crystal Explorer 3.0. Brown arrows indicate the intramolecular S…Cl interaction. The isosurfaces are drawn at 0.008 eau^{-3}.

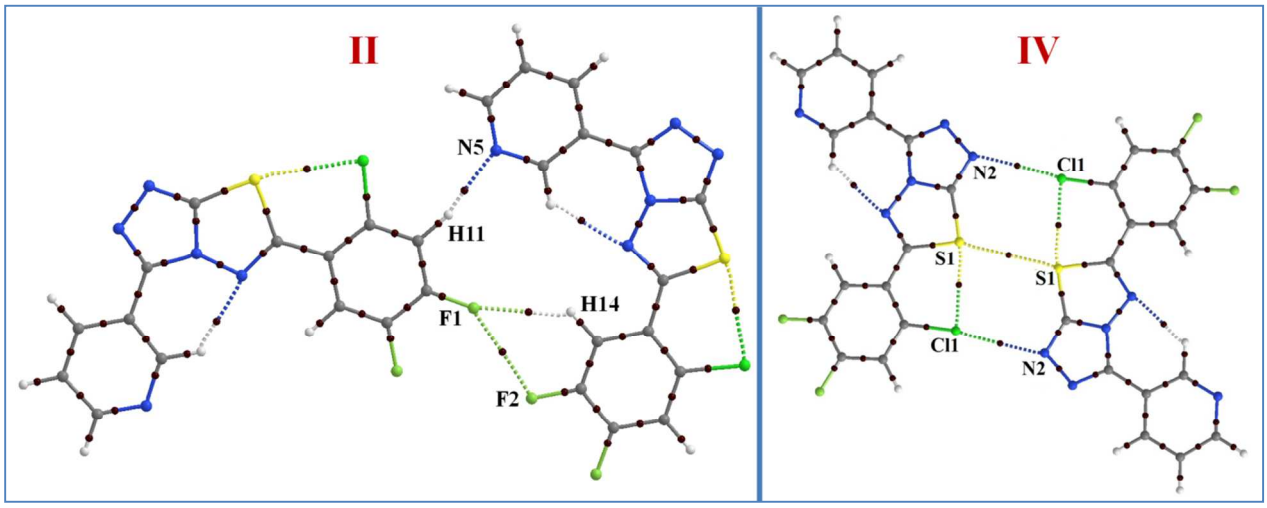

Figure 3(e): Molecule plots for motifs **II** and **IV** in **4b**, showing the presence of bond critical points (brown spheres) for different inter and intra-molecular atom-atom contacts (**Table 4**).

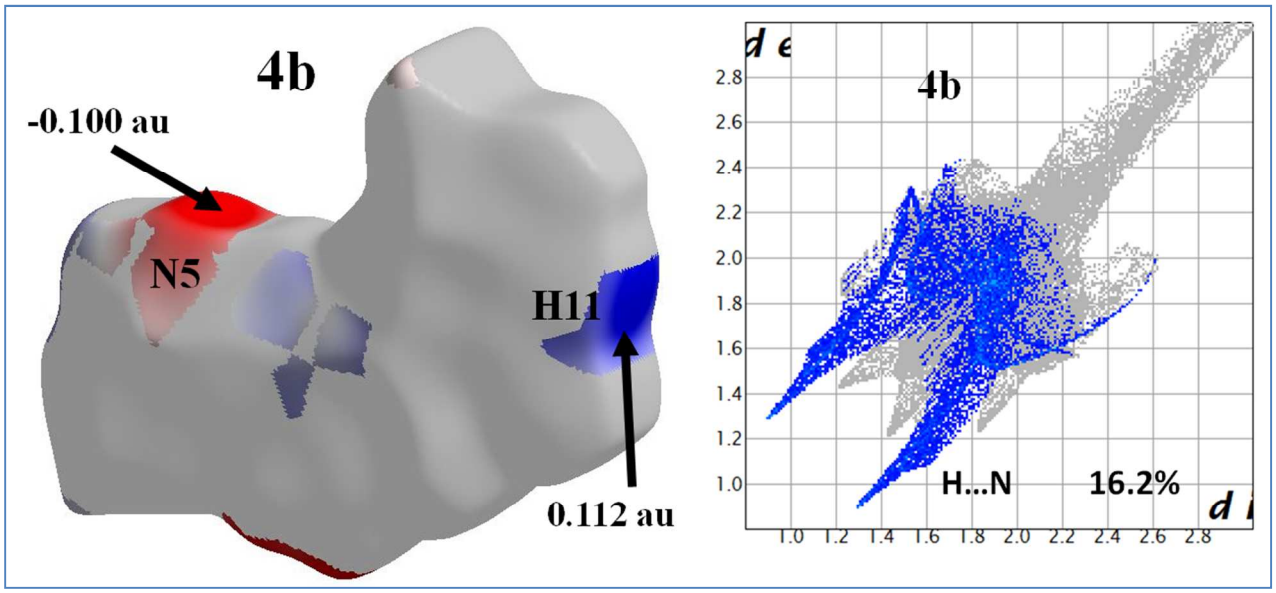

Figure 3(f): Decomposed ESP map, plotted on the Hirshfeld surface of **4b**, showing the contribution of H11···N5 contacts together with the corresponding 2D fingerprint plot.

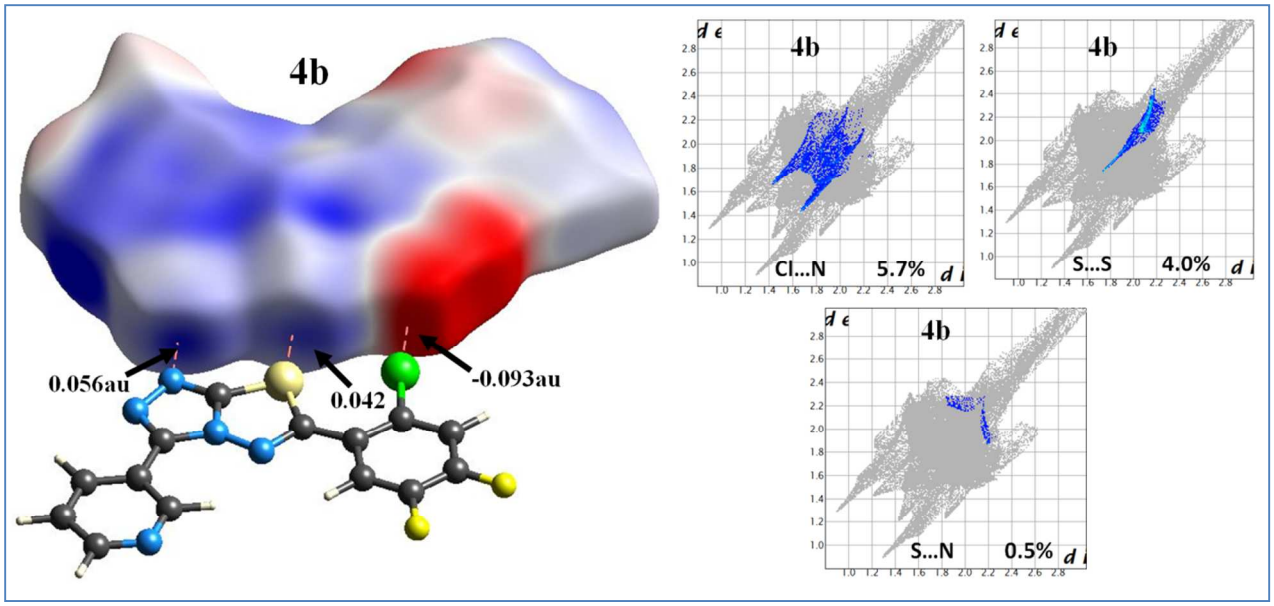

Figure 3(g): Molecular ESP mapped on the Hirshfeld surface of **4b**, displaying the Cl···N and S···S contacts along with their corresponding 2D fingerprint plots.

3.3.3. Analysis of molecular packing in 4c

The compound **4c** crystallizes in the centrosymmetric triclinic space group *P*-1 with Z=2.

Unlike **4b**, **4c** is not a planar molecule due to the replacement of the difluorochlorobenzene substituent with a *para*-fluorobenzyl group on C2 of the thiadiazole ring. However the triazolothiadiazole ring system and the pyridyl ring, with centroids Cg1, Cg2 and Cg3, remain reasonably coplanar and were found to be involved in π···π molecular stacking interactions in the crystal packing [**Fig. 4(a)**]. Such contacts provide the most stabilized motifs **I** (IE = -55.2 kJ/mol; involving a Cg2 to Cg2 contact), **III** (IE = -35.9 kJ/mol; Cg1 to Cg2) and **IV** (IE = -33.7 kJ/mol; Cg3 to Cg1) (**Table 3**).

The electrostatic potentials mapped over the Hirshfeld surfaces of both faces of the planar segments of **4c** are shown in **Fig 4(b)**. It is noteworthy that the ESP over the Cg1, Cg2 and Cg3 rings has similar characteristics to those observed in the corresponding Hirshfeld surfaces of **4b, Figs. 3(b).** The π-rings, involved in the molecular stacking, shows interactions between regions of opposite electrostatic complimentarity. Hence, the most stabilized motif **I** involves the interaction between the electropositive segment of the Cg2 ring with the complimentary electronegative part of the same ring on the oppposite surface. This results in a 48% contribution

from electrostatics towards the total stabilization energy (**Table 3**). The other two motifs **III** and **IV** were found to display 22% and 33% electrostatic contributions respectively towards their total stabilization energies. In motif **III,** a weak C1-H9A···Cg4 hydrogen bond, **Table 3** adds additional support to the Cg2···Cg1 π···π stacking interaction.

Chains of molecules parallel to the (110) plane through two sets of inversion dimers are represented by motifs **II** and **V** [**Figs. 4(c)**]. The former results from inversion related C7—H7…N4 contacts that form $R^2_2(14)$ rings[76]. These are further stabilised by C9—H9B···N5 hydrogen bonds forming $R^2_2(7)$ rings. The hydrogen atom H9B is strongly acidic on account of this being connected to two strongly electron withdrawing fluorobenzene ring and the triazolothiadiazole ring. **V** results from S1···N2 inversion dimers very similar to those found in the packing of **4a**. These chains are interconnected by very weak bifurcated C5—H5···F1 and C6—H6···F1 hydrogen bonds (motif **VI**, IE = -10.3 kJ/mol) with the formation of a molecular layer approximately parallel to (110). The C7—H7···N4 inversion dimers and C9—H9B···N5 hydrogen bonds, motif **II** (IE = -50.0 kJ/mol), represent the second most stabilized packing motifs for **4c**. The contribution to this motif from electrostatics is again significant to the extent of 49% (**Table 3**). The Hirshfeld plots focussing on these contacts show a strongly electronegative area around N5 (-0.085 au) as would be expected for a pyridine nitrogen atom. This will interact strongly with the moderately electropositive area (+0.064 au) around the acidic sp^3 hydrogen, H9B as a neighbour of the thiadiazole ring [**Fig. 4(d)**]. The second C(sp^2)—H···N hydrogen bond is revealed as a weaker interaction. This involves the acidic hydrogen, the sp^2 H7, in a moderately electopositive region (0.047au) as it is adjacent to the pyridine N5 atom. This inteacts with the weakly electropositive region about N4 (-0.025au) [**Fig. 4(d)**]. These H···N contacts display a pair of spikes on the decomposed 2D-fingerprint plot, and contribute 15.1% over the total Hirshfeld surface of **4c**.

The moderately strong motif **V** (IE = -28.2 kJ/mol) involves the formation of dimers through short S···N chalcogen bonds with a 77% contribution from electrostatics towards the total stabilization. As is observed in the case of **4a**, the motif was also observed to have a high contribution from the repulsion energy undoubtedly due to the close approach of the N2 atoms imposed by the stronger S···N chalcogen bond. ESP mapped over the Hirshfeld surface shows the presence of highly electropositive region (the 'σ-hole' 0.101 au) on the S1 atom opposite to the

C-S bond interacting with the highly electronegative region (-0.103 au) around the N2 atom [**Fig. 4(e)**]. This confirms the electrostatic origin of such chalcogen interactions. Further, topological calculations using AIMALL confirms the presence of (3, -1) BCPs for the S···N interactions and a corresponding N2···N2 BCP underscoring the repulsive contribution to the overall energy of the system [**Fig. 4(f)**, **Table 4**]. The 3D deformation density map clearly shows that the S···N chalcogen bond results from a significant interaction between the CD region on the S-atom with the CC region on the N-atom and also displays the possibility of repulsive N2···N2 contacts [**Fig. 4(g)**].

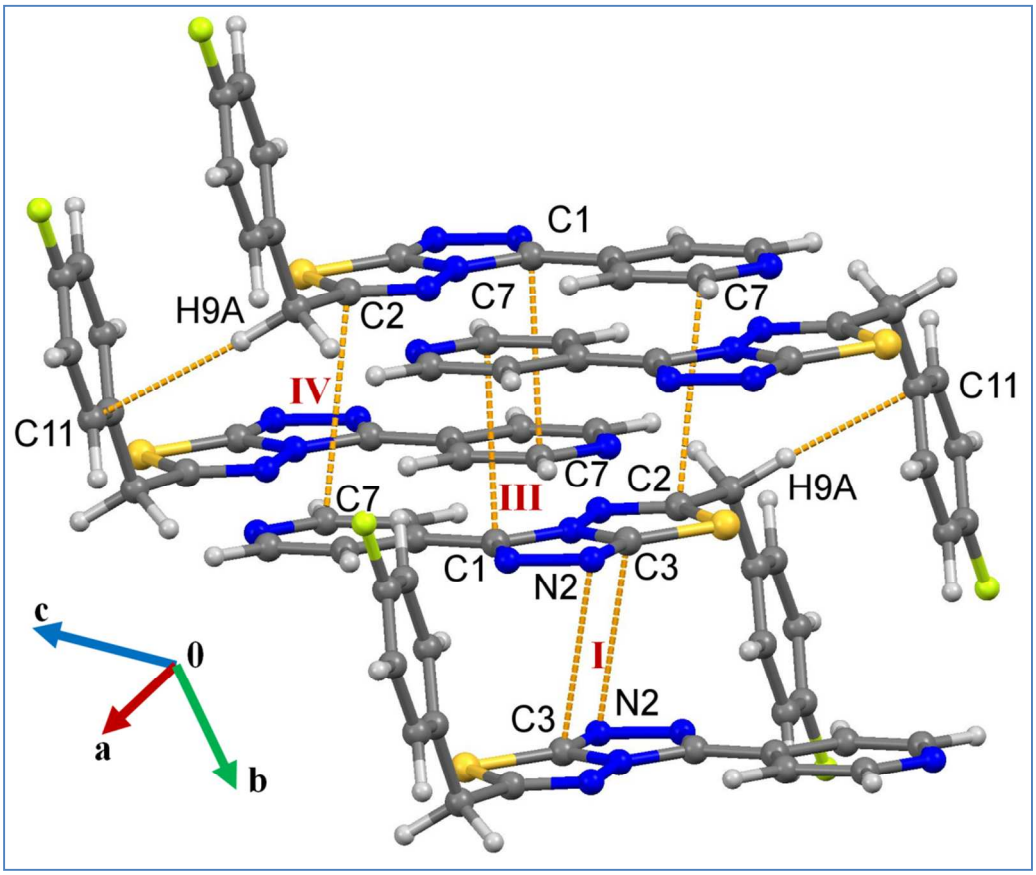

Figure 4(a): Formation of layers *via* π···π stacking along with a weak C-H···π hydrogen bond in **4c.**

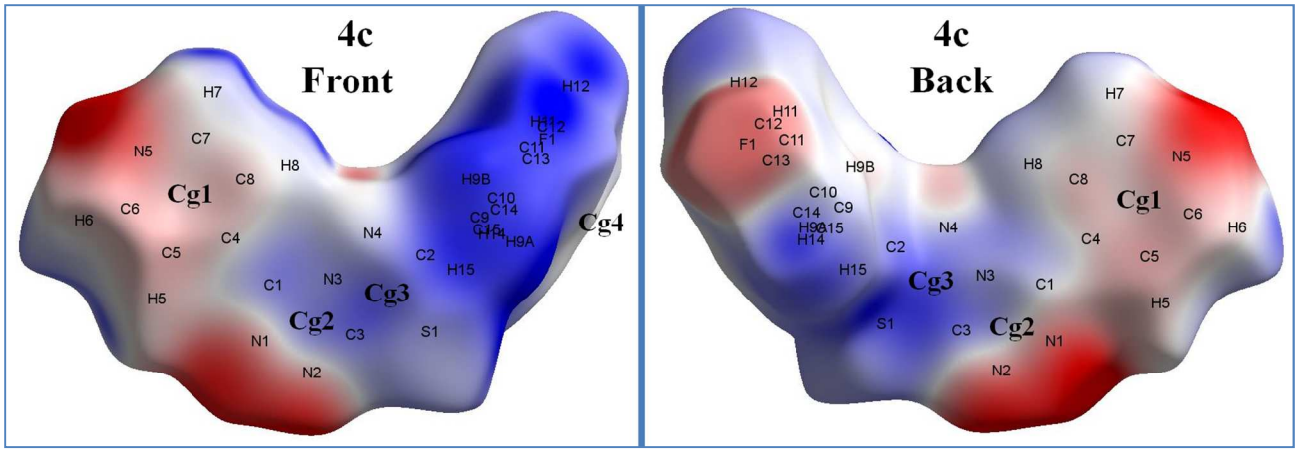

Figure 4(b): Electrostatic potential (**ESP**) mapped over the Hirshfeld surface for **4c** for the range -0.06 au (red) through 0.0 (white) to 0.06 au (blue).

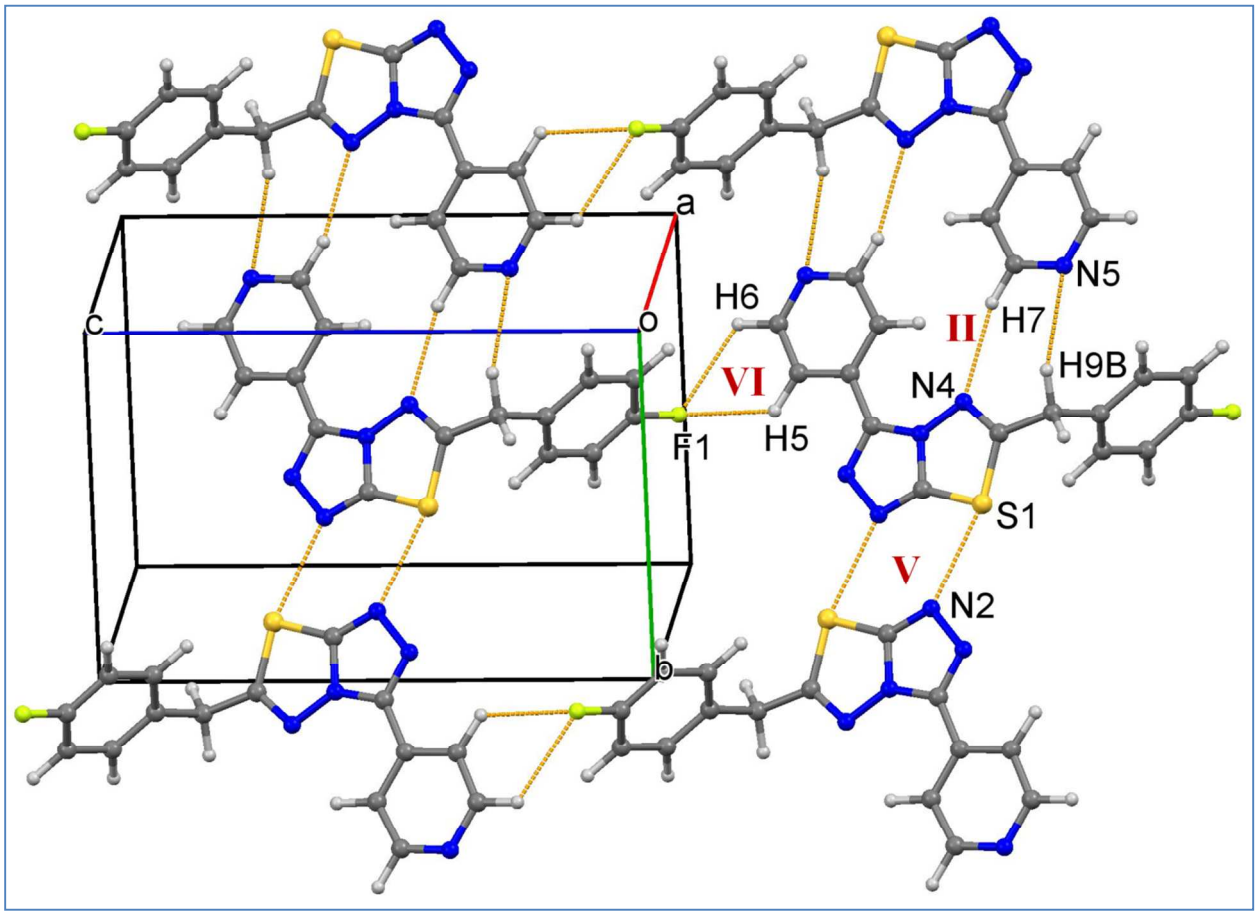

Figure 4c: Packing of molecules parallel to (110) in **4c** *via* dimeric S···N chalcogen bonds together with the weak C(sp^3)-H···N, C(sp^2)-H···N and bifurcated C(sp^2)-H···F hydrogen bonds.

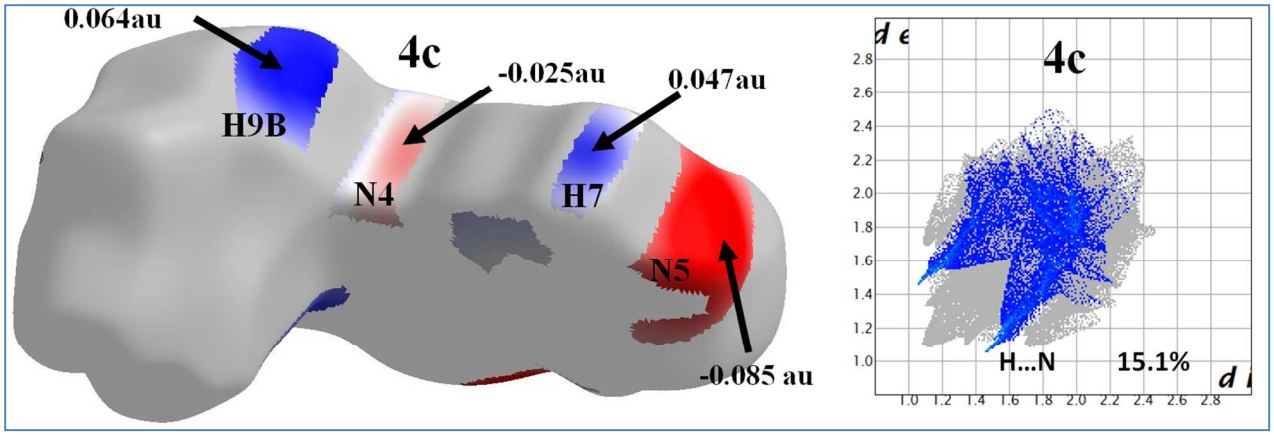

Figure 4(d): Decomposed ESP map, plotted on the Hirshfeld surface of **4c**, showing the contribution to H···N contacts along with the corresponding 2D fingerprint plot.

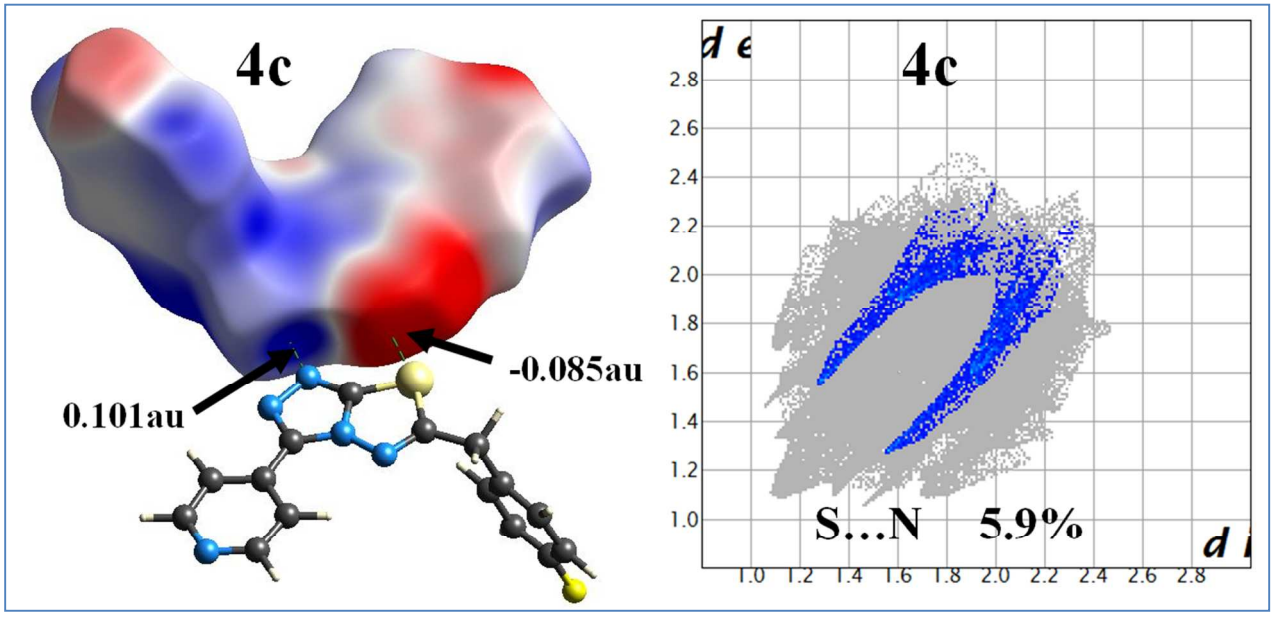

Figure 4(e): Hirshfeld surface mapped with electrostatic potential (**ESP**) for **4a** showing the σ-hole on the S-atom along with the corresponding decomposed 2D fingerprint plot for S···N contacts.

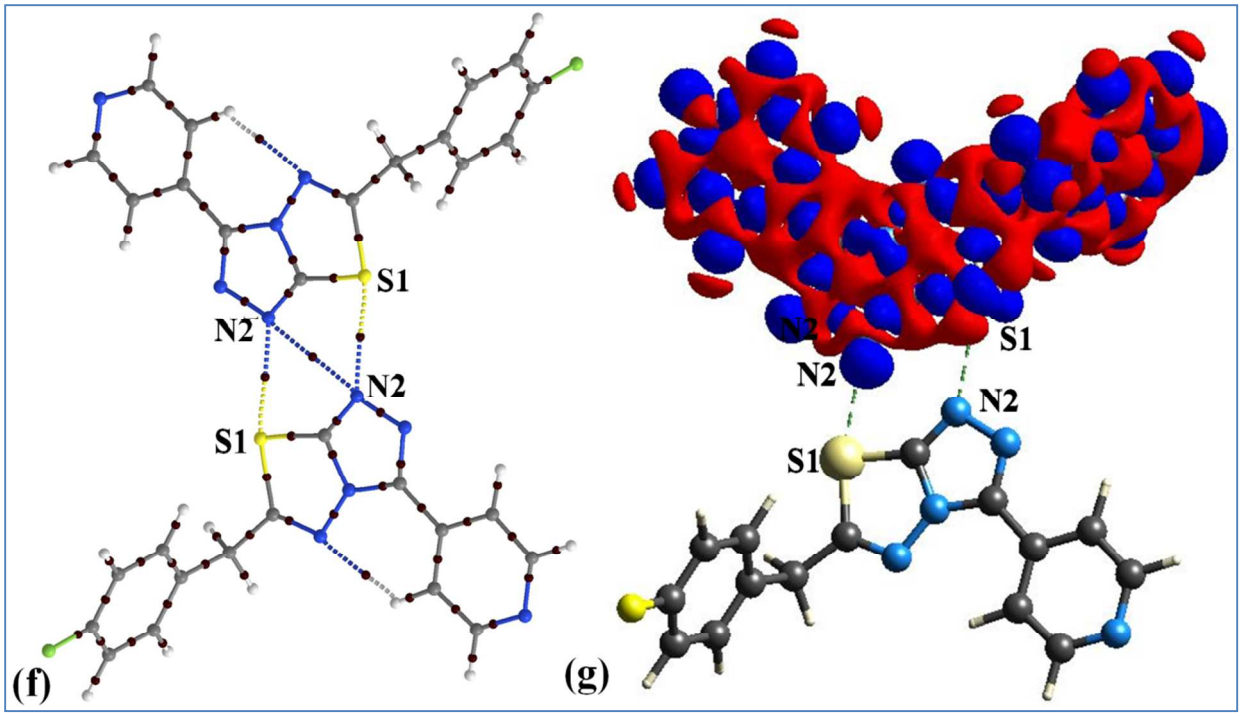

Figure 4(f): Molecular plots for the selected molecular motifs **V** in **4c**, showing the presence of (3, -1) BCPs (brown spheres) for S···N interactions (**Table 4**). **(g)** 3D-deformation density map showing the presence of CD regions (in red) and CC regions (in blue) in **4c.**

3.3.4. Analysis of the molecular packing in 4d

The compound **4d** crystallizes in the centrosymmetric orthorhombic space group *Pbcn* with Z = 8. In **4d** there is a furan ring (Cg1) on C1 of the triazole ring and a fluorobenzyl substituent on C2 of the thiadiazole ring. While the furan ring (Cg1) along with the triazolothiadiazole ring system (Cg2 and Cg3)] are almost coplanar the remaining fluorophenyl ring is almost orthogonal to that plane with a dihedral angle of 81.04(5)°. Unlike, **4a**, **4c** and **4e** (*vide infra*), the packing for **4d** is unique, relying solely on C—H···O(N) and C—H···π contacts with only very weak π···π stacking interactions with no S···N chalcogen bonds that are perhaps the most striking feature for these other structures.

ESP mapped over the Hirshfeld surface for **4d** is shown in [**Fig. 5(a)**]. The planar Cg1-Cg2-Cg3 section of the surfaces displayed similar features to those observed for **4a**. However, while Cg2···Cg3 π···π stacking interactions are possible in association with motif **1**, they are very weak,

with the Cg2···Cg3 distance being 4.4343(14) Å. However, a stronger Cg1···Cg3 contact does occur at 3.7937(13) Å.

The most stabilized contacts, motif **I**, (I.E = -46.4 kJ/mol) for **4b** result from the (sp^3)-H8B acidic hydrogen atom of the benzyl methylene group forming inversion dimers through C8—H8B…O1 hydrogen bonds with a 37% contribution from electrostatic effects. Two motifs **III** and **IV** of similar energy (IE = -25.9 kJ/mol, **Table 3**) combine with this contact to link molecules into chains along *b* [**Fig. 5(b)**]. Motif **III** evolves from C14—H14···N1 and C8—H8B···O1 hydrogen bonds with a 55% electrostatic contribution and they form $R^2_2(9)$ rings[76]. The (sp^3)-H8B hydrogen atom therefore acts as a bifurcated donor, forming two C8—H8B···O1 hydrogen bonds, one of which features in motif **1**. These hydrogen bonds generate an $R^2_2(4)$ ring motif[76] and impose a short O1···O1 contact (2.986(2) Å; symmetry operation 1-x, 1-y, 1-z) that contribute to motif **III**. Inversion dimers, again supported by the O1…O1 contact comprise motif **IV** and result from C—H···N contacts involving the acidic H7 hydrogen atom, adjacent to O1, and the N1 atom of the triazole ring, with a 67% electrostatic contribution. The ESP around the N1 atom is highly electronegative (-0.106au), **Fig. 5c**, accounting for the high electrostatic contributions to motifs **III** and **IV**, **Table 3**. In contrast such contributions to the C8—H8B…O1 contacts are more modest with values of +0.072au for H8B and -0.056au for O1, Fig. 5(c).

Three weak C—H···π hydrogen bonds, represent the second most stabilized molecular motif **II (**IE = -33.4 kJ/mol, **Table 3**), and form a chain of molecules along *b* [**Fig. 5(d)**]. Furthermore, a short and directional C11-H11···N2 hydrogen bond (motif **V**, IE = -15.4 kJ/mol) with a 61% contribution from electrostatics, owing to the presence of the highly acidic hydrogen atom H11 adjacent to the electron withdrawing fluorine atom (**Table 3**) form zig-zag chains along *a*. These chains are linked through C7-H7···F1 hydrogen bonds (motif **VI**, IE = -9.1kJ/mol), that form orthogonal set of chains along *c*. These two motifs combine to generate sheets of molecules parallel to (110) [**Fig. 5(e)**].

In order to facilitate our understanding of the absence of the short dimeric S···N chalcogen bonds, an ESP was plotted over the Hirshfeld surface [**Fig. 5(f)**]. There is clearly no strong electropositive region (σ-hole). The weakly electropositive ESP around the S-atom was calculated to be only +0.007au and hence the S···N chalcogen bond formation is not observed in **4d**.

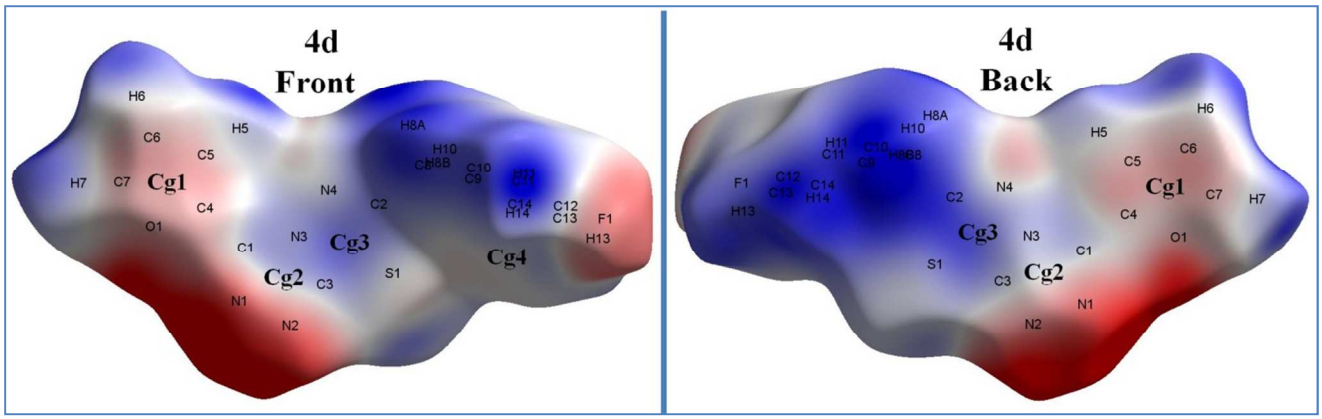

Figure 5(a): Electrostatic potential (**ESP**) mapped over the Hirshfeld surface for **4d** for the range -0.06 au (red) through 0.0 (white) to 0.06 au (blue).

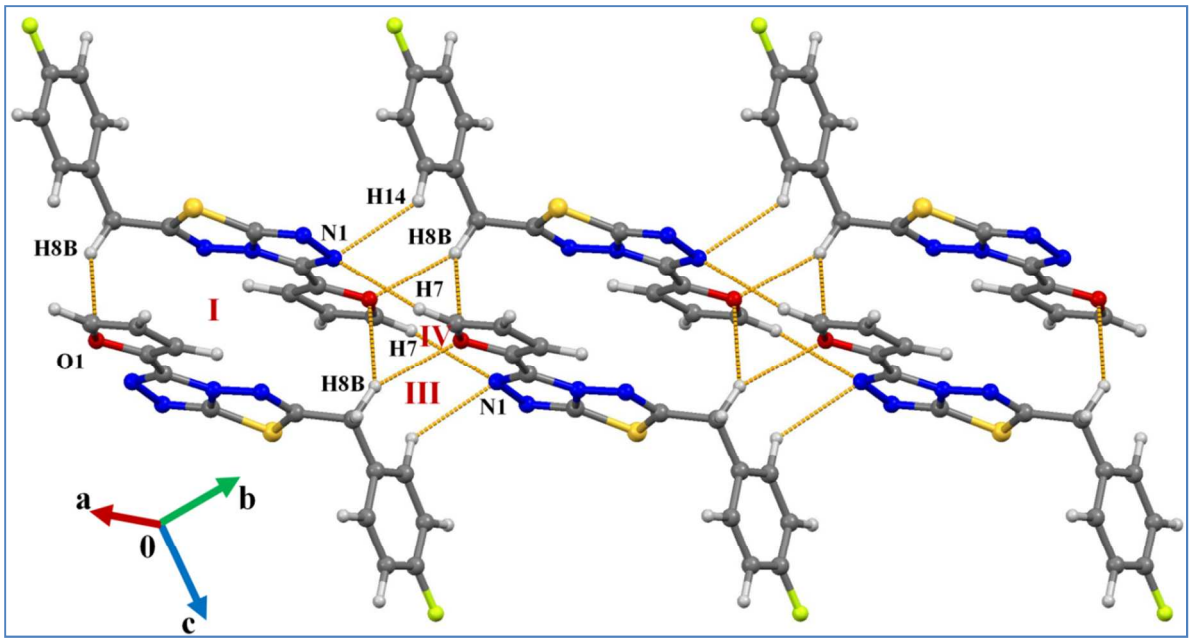

Figure 5(b): Packing of molecules *via* weak C-H···O and C-H···N hydrogen bonds in **4d**.

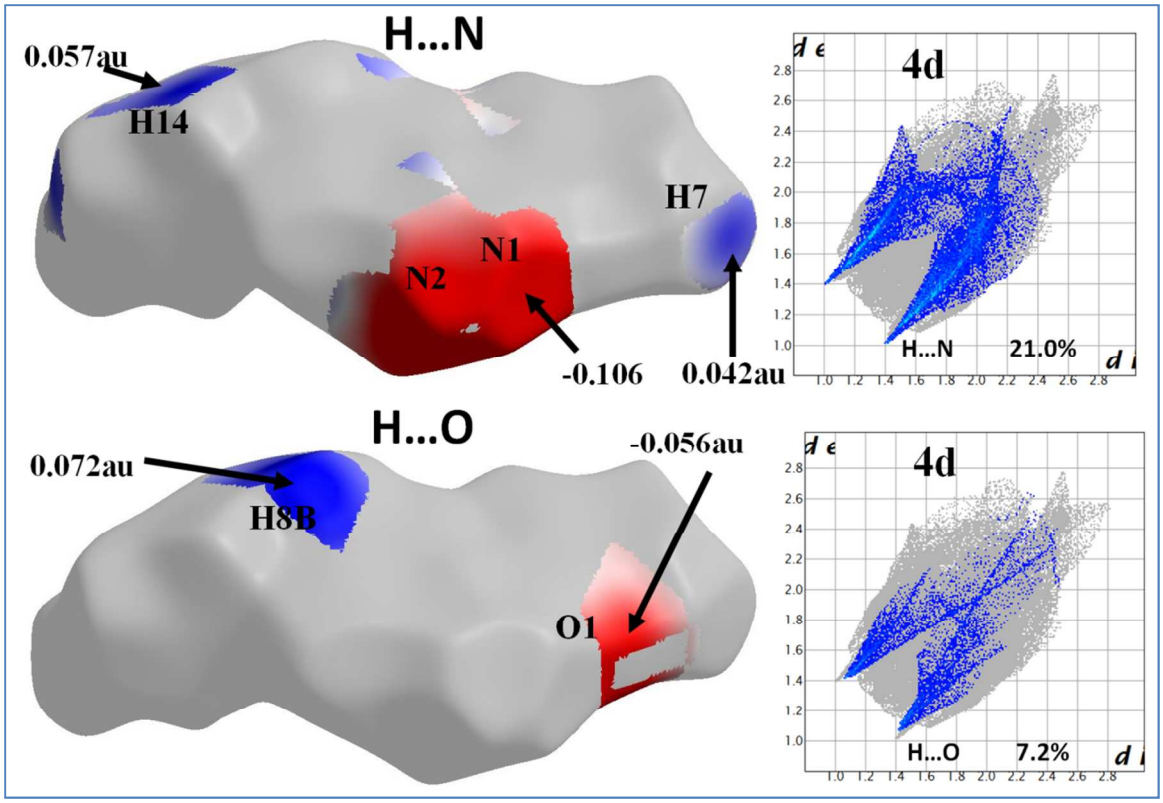

Figure 5(c): Decomposed ESP maps, plotted on the Hirshfeld surface of **4d**, showing the contribution of H···N and H···O contacts along with their corresponding 2D fingerprint plots.

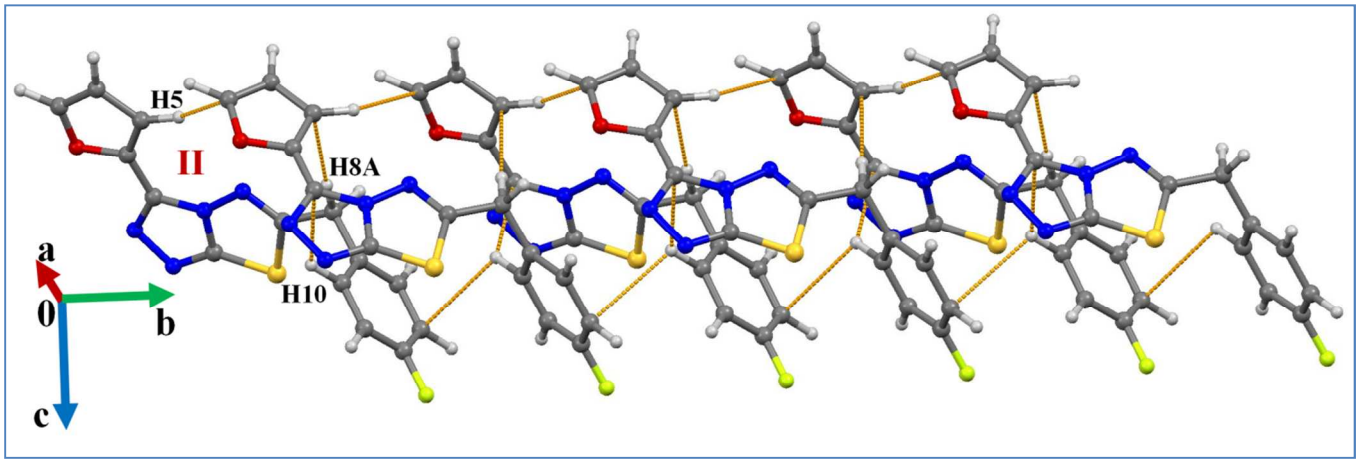

Figure 5(d): Formation of a molecular chain along the *b*-axis through C-H···π hydrogen bonds in **4d**.

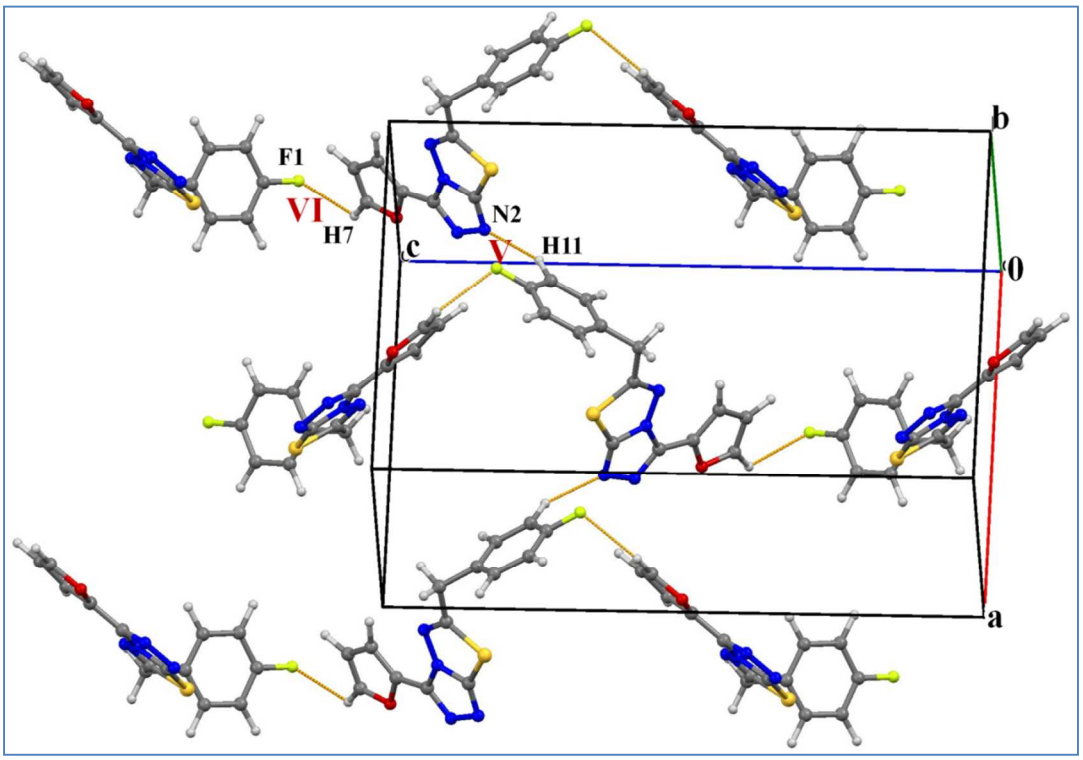

Figure 5(e): Packing view along the *ac* plane for **4d**, showing weak C-H···N and C-H···F hydrogen bonds.

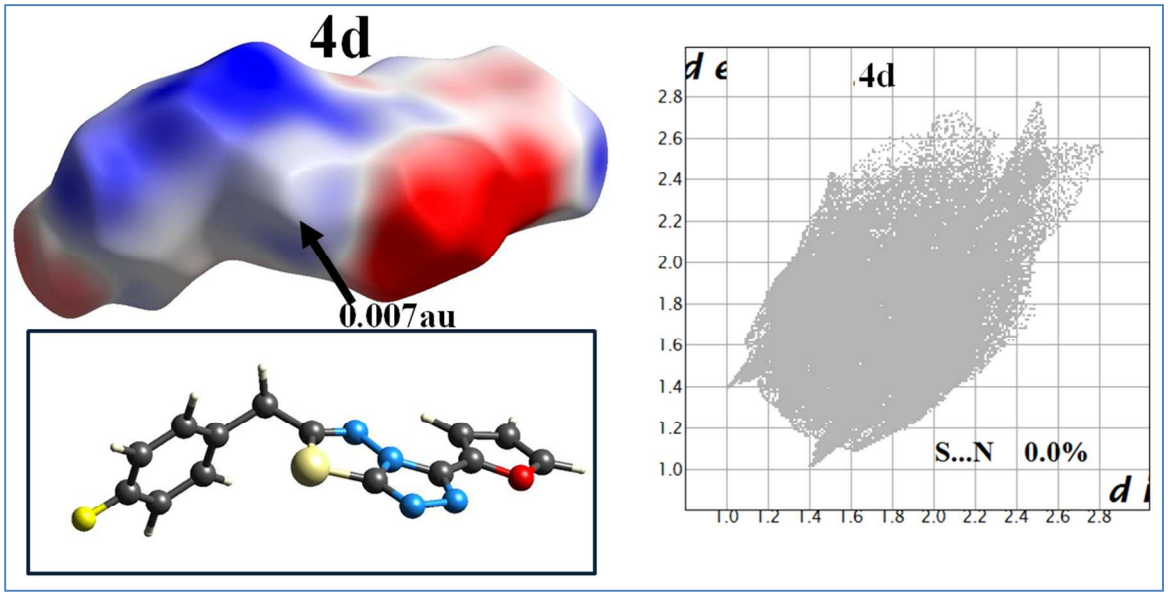

Figure 5(f): Hirshfeld surface mapped with electrostatic potential (**ESP**) for **4d** (the orientation of the molecule is shown in the box). A corresponding decomposed 2D fingerprint plot for the S···N contact is also presented.

3.3.5. Analysis of the molecular packing in 4e

The compound **4e** crystallizes in the centrosymmetric monoclinic space group $P2_1/c$ with Z = 4. The structure of **4e** is similar to that of **4c** with a pyridinyl substituent on C1 of the triazole ring but with a p-tolyloxymethyl substituent on the C2 carbon of the thiadiazole ring. The pyridyl ring is disordered over two positions, the population of the two conformers refining to the ratio of 0.572(9): 0.428(9). The tolyl ring system is also disordered over two sites with similar, but not identical occupancies, the ratio of the two conformers being 0.566(8):0.434(8). Details of the modeling of disorder is mentioned in the experimental section and in the subsequent discussion only the components involving the major disorder (labeled with a trailing 'B'), Fig 1(e), are included.

As was observed in the previous structures, the pyridine ring (Cg1) and triazolothiadiazole ring (Cg2 and Cg3) is almost coplanar with an *rms* deviation of 0.1214 Å from the mean plane passing through all 14 atoms. This planarity is supported by an intramolecular C8—H8···N4 hydrogen bond. Comparison with **4b** and **4c** in particular leads to an expectation of π···π stacking interactions in the crystal packing. The two most stabilized motifs in the crystal packing in **4e** indeed involve π···π stacking interaction (**Table 3**). A short and directional C(sp^3)-H···N hydrogen bond along with an offset π···π stacking interactions between the tolyl ring system, Cg4, and the pyridine, Cg1 and triazole, Cg2, rings contribute to the most stabilized motif **I** (IE = -42.8 kJ/mol). In addition, face to face stacking of the planar Cg1, Cg2, Cg3 segment through close inversion related Cg1···Cg3 contacts, produce the dimeric motif **II** (IE = -38.4 kJ/mol), Fig. 6(a). The contribution from electrostatics towards the total stabilization energy was found to be 37% and 33% for motif **I** and **II** respectively.

Inversion related S···N chalcogen bonds appear again for **4e** (motif **III**, IE = -33.0 kJ/mol) with a 75% contribution from electrostatics towards the total stabilization energy of this contact. A high repulsion term again reflects the close approach of the N2 atoms, 3.029(2) Å, in the dimers imposed by the chalcogen bond formation. Motifs **II** and **III** combine to form chains of molecules propagating along the crystallographic *b*-axis [**Fig. 6(a)**].

The first three most stabilized molecular motifs were observed to be connected to one another *via* short C(sp^2)-H···N hydrogen bonds involving acidic hydrogen atoms forming motifs **IV** (-23.4 kJ/mol) and **VI** (-12.9 kJ/mol) [**Fig. 6(a)**, **Table 3**]. The motif **IV** was observed to involve the interaction of the acidic hydrogen, H11B, with the *lp* of the pyridyl nitrogen, N5B, and exhibits a 54% contribution from electrostatics (**Table 3**).

Short C—H···N hydrogen bonds involving acidic hydrogens constitute motifs **IV** (-23.4 kJ/mol) and **VI** (-12.9 kJ/mol). In **IV** the pyridine N5B atom acts as a bifurcated acceptor forming C9—H9B···N5 and C11B—H11B···N5B hydrogen bonds that generate $R^1_2(7)$ rings[76]. These link the **4e** molecules in a head-to-tail fashion into chains along *c* [**Fig. 6(b)**].

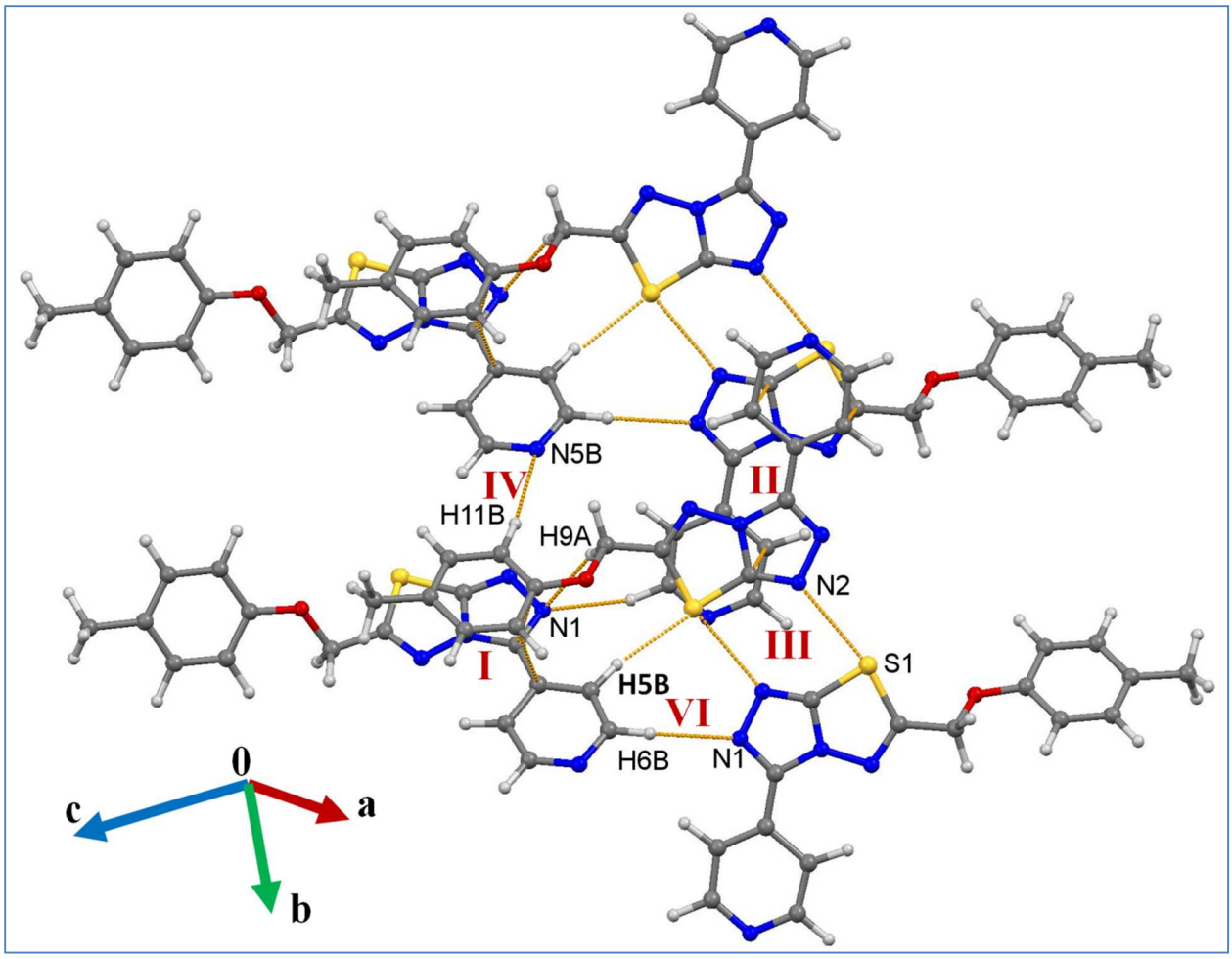

Figure 6(a): Packing of molecules *via* a network of π···π contacts, S···N chalcogen bonds and weak C(sp^3)/(sp^3)-H···N and C-H···S hydrogen bonds in **4e**.

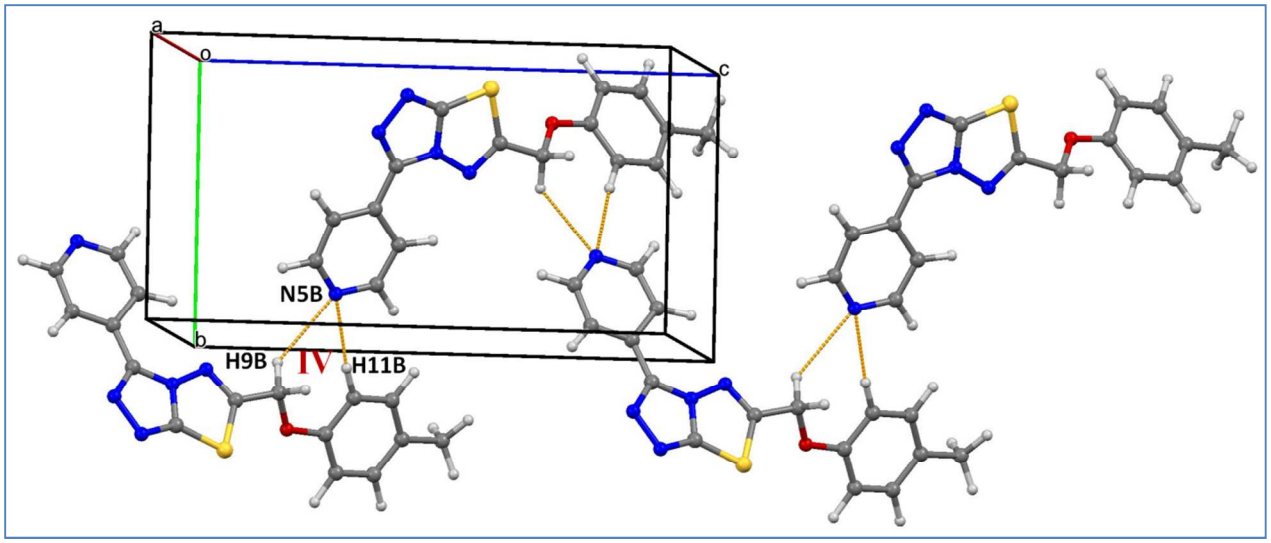

Figure 6(b): Formation of molecular chains along the *c*-axis through bifurcated C—H…N hydrogen bonds in **4e**.

Chains are also produced by motif **VI** through C6B—H6B···N1 hydrogen bonds that form zig-zag C(6) chains[42] along *b*-axis. These combine with C15B—H15B···Cg4 contacts to generate sheets in the *bc* plane, **Fig 6(c)**.

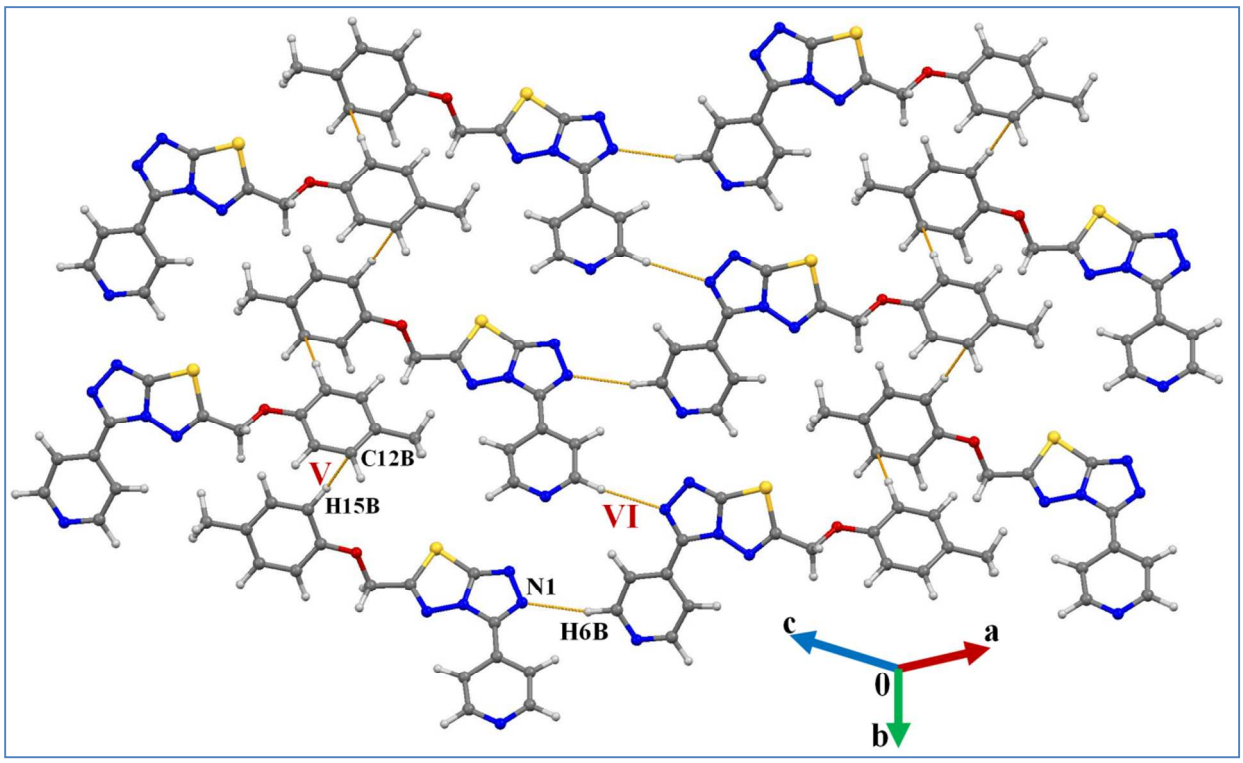

Figure 6(c): Packing of molecules in the (101) plane in **4e** through weak C--H···π and C--H···N hydrogen bonds.

3.3.6. Overview of the molecular packing for 4a—4e

A detailed analysis of the crystal packing and intermolecular interactions in these compounds through investigations using different computational approaches reveals the following significant points:

(i) Mapping electrostatic potentials (ESP) over the Hirshfeld surfaces of molecular systems is useful in exploring the electrostatic complementarity that exists in the crystal packing between differently substituted molecular skeletons. Equally useful is the determination of the high electrostatic contribution to packing interactions through PIXEL energy calculations to show where regions of opposite electrostatic complementarity interact.

(ii) The role of dispersion forces and electrostatics has been addressed by many researchers, using data from a variety of different theoretical models, to analyze the role of intermolecular π···π stacking[84-89]. Hunter and Sanders proposed the electrostatic model[84] for this interaction which suggests that both T-shaped and offset geometry are two favourable arrangements for π-contacts. This theory, however, was further questioned by many researchers as the effects of dispersion had not been considered in this model[90-91]. SAPT[92] analysis on the model system (parallel stacking of benzene rings) shows that the principal contribution to the total stabilization comes from dispersion[91]. This was also observed to be valid when one of the interacting rings were substituted with an electron donating group, whereas presence of an electron withdrawing substituent on one ring increases the contribution from electrostatics[87, 91].

In the current work it was clearly demonstrated that, in cases where the molecular surfaces had significantly disparate electrostatic regions, π···π molecular stacking interactions showed a significant contribution from electrostatics (generally an electrostatic contribution to an extent of 48% were observed). However, if there were no significant differences in the electrostatic nature of the interacting molecular surfaces, it is dispersion forces that contribute most significantly to the total stabilization (generally by more than 90%).

(iii) A prominent feature of the packing for three of the thiadiazole derivatives reported here, **4a, 4c** and **4e**, is the formation of inversion dimers derived from S···N chalcogen bonds. Analysis of the ESP, mapped over the Hirshfeld surface, confirms in each case that these contacts result from the interaction between a strongly electropositive σ-hole on the sufur atom with an electronegative region on the N atom with a contribution in excess of 70% from electrostatics as calculated by the PIXEL method. Another influence on the packing of these molecules that

emerges from these calculations was that, while the electrostatic potentials about N and O atoms were reasonably constant, the electropositive potential around the sulfur atom varied widely with values ranging from +0.101 *au* in **4c** to 0.007*au* in **4d** leading to variations in the nature of the packing motifs. In the case of **4d**, the weakly electropositive region around the S-atom precludes the formation of an S···N chalcogen bond or indeed any other significant contact.

(iv) QTAIM based calculations, shows the presence of a (3, -1) BCP for the intermolecular S···N chalcogen bond, the topological parameters at the BCP are ρ(bcp) = 0.14 e/Å^3, Laplacian ($\nabla^2\rho_{BCP}$) = 1.47 e/Å^5 for R_{ij} = 2.81Å. To the best of our knowledge, there are no previous reports on the topological analysis of short S···N contacts *via* experimental electron density studies. The stabilization energy, calculated using an EML approach[68] is ~18 kJ/mol for each contact investigated. This correlates well with the previous report by Adhikari and Scheiner[93]. The deformation density plots confirm the presence of strong interactions between charge depletion (CD) regions on the S atoms and charge concentration (CC) regions around the N atoms resulting in S···N chalcogen bond formation.

4. Conclusions

Five biologically active triazolothiadiazole derivatives have been synthesized and these have been investigated for the presence of different unique supramolecular features using a combination of experimental and computational procedures. It is observed that the packing of the molecules is sensitive towards the nature of substitents present on the triazolothiadiazole scaffold. A feature of the molecular structures of all 5 molecules is the planarity of the cyclic segments of the molecules that disposes the molecules to π···π stacking interactions in their crystal strcutures. The unique supramolecular feature established from the current study is the existence of short inversion related S···N chalcogen bonds, Cl···N halogen bonds, and this has been quantitatively characterized via inputs from ESP and 3D deformation density maps. The presence of (3, -1) BCPs obtained from an analysis of the topological properties for these interactions further confirm their presence in the crystal packing. Quantitative analysis of the packing in all five crystal structures (insights from PIXEL energy calculations) shows that the packing is stabilized by the presence of a variety of weak interactions including C—H···O, C—H···N and C—H···π hydrogen bonds together with π···π stacking interactions. Further

investigation shall be aimed towards the modulation of the electrostatic complementarity between the interacting rings by the incorporation of different atoms or substituents on the molecular scaffold.

To finally conclude, it is clear from this investigation that the combination of PIXEL energy calculations, mapping ESP over the Hirshfeld surface, 2D fingerprint plots, 3D-deformation density maps and QTAIM calculations on bond critical points provide a particularly powerful set of tools to use in investigations of crystal packing in small organic molecules.

Acknowledgements

The authors would like to sincerely appreciate the Deanship of Scientific Research at the King Saud University for funding this research through the Prolific Research Group, Project No. PRG-1436-18. PP thanks UGC-India for research scholarship. DC and PP thank IISER Bhopal for research facilities and infrastructure. We also thank the University of Otago for purchase of the diffractometer.

References

1. Philip, D.; Stoddart, J. F. *Angew. Chem., Int. Ed.* **1996**, *35*, 1154−1196.
2. Cerny, J.; Hobza, P. *Phys. Chem. Chem. Phys*. **2007**, *9*, 5291−5303.
3. Desiraju, G. R. *J. Am. Chem. Soc.* **2013**, *135*, 9952−9967.
4. Persch, E.; Dumele, O.; Diederich, F. *Angew. Chem., Int. Ed*. **2015**, *54*, 3290−3327.
5. Nangia A.; Desiraju, G. R. in *Design of Organic Solids*, ed. Weber, E. Springer-Verlag, Berlin, **1998.**
6. Desiraju, G. R. *Angew. Chem., Int. Ed*. **2011**, *50*, 52−59.
7. Desiraju, G. R. *Chem. Commun*. **2005**, 2995−3001.
8. Bosch, E. *Cryst. Growth Des.* **2010**, *10*, 3808−3813.
9. Takahashi, O.; Kohno, Y.; Nishio, M. *Chem. Rev*. **2010**, *110*, 6049−6076.
10. Nishio, M. *Phys. Chem. Chem. Phys*. **2011**, *13*, 13873−13900.
11. Desiraju, G. R.; Steiner, T. *The Weak Hydrogen Bond in Structural Chemistry and Biology; Oxford University Press: Oxford,* **1999**.
12. Arunan, E.; Desiraju, G. R.; Klein, R. A.; Sadlej, J.; Scheiner, S.; Alkorta, I.; Clary, D. C.; Crabtree, R. H.; Dannenberg, J. J.; Hobza, P.; Kjaeergaard, H. G.; Legon, A. C.; Mennucci, B.; Nesbitt, D. J. *Pure Appl. Chem*. **2011**, *83*, 1619−1636.

13. Arunan, E.; Desiraju, G. R.; Klein, R. A.; Sadlej, J.; Scheiner, S.; Alkorta, I.; Clary, D. C.; Crabtree, R. H.; Dannenberg, J. J.; Hobza, P.; Kjaeergaard, H. G.; Legon, A. C.; Mennucci, B.; Nesbitt, D. J. *Pure Appl. Chem*. **2011**, *83*, 1637−1641.

14. Riley, K. E.; Hobza, P. *Acc. Chem. Res*. **2013**, *46*, 927−936.

15. Saraogi, I.; Vijay, V. G.; Das, S.; Sekar K.; Guru Row, T. N. *CrystEngComm*, **2003**, *6*, 69.

16. Egli M,; Sarkhel S.; *Acc Chem Res*. **2007**, *40*, 197-205.

17. Mooibroek, T. J.; Gamez, P. and Reedijk J.; *CrystEngComm*, **2008**, *10*, 1501-1515.

18. Metrangolo, P.; Resnati, G.; Pilati, T.; Biella, S. *In Halogen Bonding: Fundamentals and Applications;* Metrangolo, P., Resnati, G., Eds.; Springer-Verlag: Berlin, **2008**; *126*, 105−136.

19. Priimagi, A.; Cavallo, G.; Metrangolo, P.; Resnati, G. *Acc. Chem. Res*. **2013**, *46,* 2686−2695.

20. Wang W.; Ji, B.; Zhang Y.; *J. Phys. Chem. A* **2009**, *113,* 8132–8135.

21. Thomas, S. P.; Satheeshkumar K.; Mugesh, G.; Guru Row T. N.; *Chem. Eur. J.* **2015**, *21*, 6793 – 6800.

22. Brezgunova, M. E.; Lieffrig, J.; Aubert, E.; Dahaoui, S.; Fertey, P.; Lebegue, S.; Angyan, J. G.; Fourmigue, M.; Espinosa, E. *Cryst. Growth Des*. **2013**, *13*, 3283–3289.

23. Pavan, M. S.; Jana, A. K.; Natarajan, S.; Guru Row, T. N. *J. Phys. Chem. B*, **2015**, DOI: 10.1021/acs.jpcb.5b03533.

24. Murray, J. S.; Lane, P.; Clark, T.; Politzer, P. *J. Mol. Model*. 2007, **13**, 1033 – 1038.

25. Burling, F.T.; Goldstein, B.M. *J. Am. Chem. Soc*. 1992, **114**, 2313 – 2320.

26. Brinck, T.; Murray, J.S.; Politzer, P. *Int. J. Quantum Chem*. 1992, **44**, 57–64.

27. Murray, J. S.; Lane, P.; Politzer, P. *Int. J. Quant. Chem.*, 2007, **107**, 2286 – 2292

28. Murray, J. S.; Lane, P.; Politzer, P. *J. Mol. Model*. 2009, **15**, 723 – 729.

29. Politzer, P.; Murray, J. S.; Clark, *Phys. Chem. Chem. Phys*. **2013**, *15*, 11178−11189.

30. Desiraju, G. R.; Ho, P. S.; Kloo, L.; Legon, A. C.; Marquardt, R.; Metrangolo, P.; Politzer, P.; Resnati, G.; Rissanen, K. *Pure Appl. Chem*. **2013**, *85*, 1711−1713.

31. Thomas, S. P.; Pavan M. S.; Guru Row T. N.; *Chem. Commun.*, **2014**, 50**,** 49-51.

32. Politzer, P.; Murray, J. S.; Janjić, G. V.; Zarić, S. D. *Crystals*, 2014, **4**, 12 – 31.

33. George, J.; Deringer, V. L.; Dronskowski R.; *J. Phys. Chem. A* **2014**, *118*, 3193−3200.

34. Polshettiwar, V.; Varma, R. S. *Curr. Opin. Drug Discovery Dev*. **2007**, *10*, 723–737.

35. McGrath, N. A.; Brichacek, M.; Njardarson, J. T. *J. Chem. Educ*. **2010**, *87*, 1348-1349.

36. Purohit, D. H.; Dodiya, B. L.; Ghetya, R. M.; Vekariya, P. B.; Joshi, H. S. *Acta Chim. Slov*. **2011**, *58*, 53-59.

37. Varvaresou, A.; Siatra-Papastaikoudi, T.; Trotinis, A.; Tsantili-Kakoulidou, A.; Vamvakides, A. *Farmaco*. **1998**, *53*, 320-326.

38. Kaplancikli, Z. A.; Turan-Zitouni, G.; Oezdemir, A.; Revial, G.; *Eur. J. Med. Chem*. **2008**, *43*, 155-159.

39. Foroumadi, A.; Mirzaei, A.; Shafiee, A. *Pharmazie*. **2001**, *56*, 610-612.

40. Zou, X. J.; Jin, G.Y.; Zhang, Z. X. *J. Agric. Food Chem*. **2000**, *48*, 5312-5315.

41. Ammar, Y. A.; Ghorab, M. M.; El-Sharief, A. M. S.; Mohamed, S. I.; *Heteroat. Chem*. **2002**, *13*, 199-206.

42. Heindel, N. D.; Reid, J. R.; *J. Heterocycl. Chem.* **1980**, *17*, 1087-1088.

43. Boschelli, D. H.; Connor, D. T.; Kostlan, C. R.; Kramer, J. B.; Mullican, M. D.; Sircar, J. C. *US 5*, **1992**, **April 7**, *102*, 897.

44. Kamal, A.; Khan, M. N. A.; Srikanth, Y. V. V.; Reddy, K. S.; Juvekar, A.; Sen, S.; Kurian, N.; Zingde, S. *Bioorg. Med. Chem*. **2008**, *16*, 7804-7810.

45. Skoumbourdis, A. P.; LeClair, C. A.; Stefan, E.; Turjanski, A. G.; Maguire, W.; Titus, S. A.; Huang, R.; Auld, D. S.; Inglese, J.; Austin, C. P.; Michnick, S. W.; Xia, M.; Thomas, C. J.; *Bioorg. Med. Chem. Lett.* **2009**, *19*, 3686-3692.

46. Lauffer, D.; Li, P.; Mcginty, K. *EP 2 435 443 B1*, July 31, **2013.**

47. El-Shehry, M. F.; Abu-Hashem, A. A.; El-Telbani, E. M. *Eur. J. Med. Chem*. **2010**, *45*, 1906-1911.

48. Zhang, L. X.; Zhang, A. J.; Chen, X. X.; Lei, X. X.; Nan, X. Y.; Chen, D. Y.; Zhang, Z. Y. *Molecules*. **2002**, *7*, 681–689.

49. Rafiq, M.; Saleem, M.; Hanif, M.; Maqsood, M. R.; Rama, N. H.; Lee, K.-H.; Seo, Bull. S.-Y. *Korean Chem. Soc.* **2012**, *33*, 3943-3949.

50. Khan, I.; Ibrar, A.; Zaib, S.; Ahmad, S.; Furtmann, N.; Hameed, S.; Simpson, J.; Bajorath, J.; Iqbal, J. *Bioorg. Med. Chem.* **2014,** *22***,** 6163-6173.

51. Khan, I.; Zaib, S.; Ibrar, A.; Rama, N. H.; Simpson, J.; Iqbal, J. *Eur. J. Med. Chem*. **2014**, *78*, 167-177.

52. Khan, I.; Hameed, S.; Abdul-Reda, N. A.; Al-Masoudi, N. A.; Simpson, J. Z. *Naturforschung B*, **2015**, *70*, 47-58.

53. Bruker. *APEX2*, *SAINT* and *SADABS*. Bruker AXS Inc.: Madison, Wisconsin, USA, 2011.

54. Sheldrick, G. M. *Acta Crystallogr., Sect. A*: *Fundam. Crystallogr*. **2008**, *64*, 112−122.

55. Sheldrick, G. M. *Acta Crystallogr., Sect. C: Struct. Chem*. **2015**, *71*, 3−8.

56. Hunter, K. A.; Simpson, J. **1999**. *TITAN2000*. University of Otago, New Zealand.

57. Macrae, C. F.; Bruno, I. J.; Chisholm, J. A.; Edgington, P. R.; McCabe, P.; Pidcock, E.; Rodriguez-Monge, L.; Taylor, R.; Streek, J.; Wood, P. A. *J. Appl. Crystallogr.* **2008**, *41*, 466−470, www.ccdc.cam.ac.uk/mercury.

58. Spek, A. L. *Acta Crystallogr., Sect. D: Biol. Crystallogr*. **2009**, *65*, 148-155.

59. Gavezzotti, A.; *Mol.Phys.* **2008**, *106*, 1473-1485.

60. Frisch, M. J., *et al.*, *Gaussian 09, Revision A.02*, Gaussian, Inc., Wallingford CT, **2009**.

61. Panini, P.; Venugopala, K. N.; Odhav, B.; Chopra, D. *Acta Cryst.* **2014**, *B70*, 681–696.

62. Wolff, S.K.; Grimwood, D.J.; McKinnon, J.J.; Turner, M.J.; Jayatilaka, D.; Spackman, M.A. *CrystalExplorer, Version 3.0*; University of Western Australia, 2012.

63. Spackman, M.A.; Jayatilaka, D. *CrystEngComm*. **2009**, *11*, 19 – 32.

64. Spackman, M. A; McKinnon, J. J.; Jayatilaka D. *CrystEngComm*. **2008**, *10*, 377 – 388.

65. Bader, R. F. W. *Atoms in Molecules: A Quantum Theory;* Oxford University Press: Oxford, U.K., **1990**.

66. Popelier, P. L. *Atoms in Molecules: An Introduction;* Prentice Hall: London, **2000**.

67. Keith, T. A. *AIMALL*, version 13.05.06; TK Gristmill Software, Overland Park KS, USA, **2013**; aim.tkgristmill.com.

68. Espinosa, E.; Molins, E.; Lecomte, C. *Chem. Phys. Lett*. **1998**, *285*, 170−173.

69. Groom, C. R.; Allen, F. H. *Angew. Chem. Int. Ed*. **2014**, 53. 662—671.

70. Wang, D. –Z.; Zhang, Q.; Zhang, J. –B.; Wu, Y. –G.; Cao, L. –H.; Ma P. –Y. *Polyhedron*, **2012**, *42*, 216 - 226.

71. Shen, X. –Q.; Yang, R.; Yao, H. –C.; Zhang, H. –Y.; Li, G.; Zhang, H. –Q.; Chen, P. –K.; Hou H. –W. *J Coord. Chem*. **2006,** *59*, 2031 - 2038.

72. Lu, D.; Zhang, M.; Song, L.; Tan, Q.; Shao, M. *Acta Cryst.* **2008**, *E64*, o80.

73. Rowland, R. S.; Taylor, R. *J. Phys. Chem.* **1996**, *100*, 7384 –7391.

74. Panini, P.; Shukla, R.; Mohan, T. P.; Vishalakshi, B.; Chopra, D. *J. Chem. Sci.* **2014**, *126*, 1337–1345.

75. Tsuzuki, S.; Sato, N.; *J. Phys. Chem. B*. **2013**, *117*, 6849−6855.

76. Bernstein, J.; Davis, R.E.; Shimoni, L.; Chang, N. -L. *Angew. Chem. Int. Ed. Engl.* **1995**, *34*, 1555-1573.

77. Grimme, S. *Angew. Chem. Int. Ed.* **2008**, *47*, 3430 –3434.

78. P. Panini and D. Chopra, *Cryst.Growth Des.* **2014**, *14*, 3155−3168.

79. Panini, P.; Chopra, D.; In *Hydrogen Bonded Supramolecular Structures*, Eds. Z. Li and L.Wu, *Lecture Notes in Chemistry,* **2015**, *87*, 37 -67. Springer-Verlag, Berlin, Heidelberg.

80. Hathwar, V. R.; Chopra, D.; Panini, P.; Guru Row, T. N. *Cryst. Growth. Des.* **2014**, *14*, 5366–5369.

81. Hathwar, V. R.; Guru Row, T. N. *Cryst. Growth Des.* **2011**, *11*, 1338−1346.

82. Bai, M; Thomas, S. P.; Kottokkaran, R.; Nayak, S. K.; Ramamurthy, P. C.; Guru Row, T. N. *Cryst. Growth Des.* **2014**, *14*, 459−466.

83. Thomas, S. P.; Prasad, S.; Veccham, K. P.; Farrugia, L. J.; Guru Row, T. N. *Cryst. Growth Des.* **2015**, *15*, 2110−2118.

84. Hunter, C. A.; Sanders, J. K. M. *J. Am. Chem. Soc.* **1990**, *112,* 5525-5534.

85. Cockroft, S. L.; Hunter, C. A.; Lawson, K. R.; Perkins, J.; Urch, C. J. *J. Am. Chem. Soc.* **2005**, *127*, 8594-8595.

86. Wheeler, S. E. *Acc. Chem. Res*. **2013**, *46*, 1029–1038.

87. Wheeler, S. E. *J. Am. Chem. Soc.* **2011**, *133*, 10262–10274.

88. Bloom, J. W. G.; Wheeler, S. E. *Angew. Chem., Int. Ed*. **2011**, *50*, 7847 –7849.

89. Mathew, S. M.; Engle, J. T.; Ziegler, C. J.; Hartley, C. S. *J. Am. Chem. Soc.* **2013**, *135*, 6714−6722.

90. Sherrill, C. D. *Acc. Chem. Res*. **2013**, *46*, 1020–1028.

91. Pace, C. J.; Gao, J. *Acc. Chem. Res.* **2013**, *46*, 907–915.

92. Szalewicz, K. *Symmetry-adapted perturbation theory of intermolecular forces*. *Wiley Interdiscip. Rev.: Comput. Mol. Sci*. **2012**, *2*, 254–272.

93. Adhikari U.; Scheiner, S. *J. Phys. Chem. A* **2014**, *118*, 3183−3192.

For Table of Contents only:

Exploiting the role of molecular electrostatic potential, deformation density, topology and energetics in the characterization of S···N and Cl···N supramolecular motifs in crystalline triazolothiadiazoles

Imtiaz Khan, Piyush Panini, Salah Ud-Din Khan, Usman Ali Rana, Hina Andleeb, Deepak Chopra, Shahid Hameed, Jim Simpson

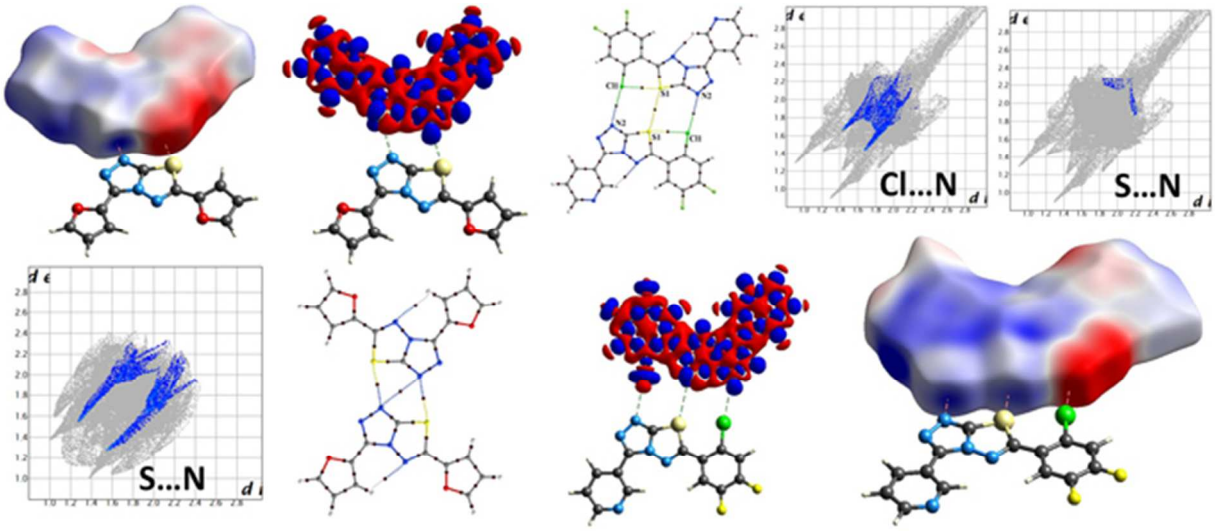

The combination of PIXEL energy calculations, mapping ESP over the Hirshfeld surface, 2D fingerprint plots, 3D-deformation density maps and QTAIM calculations were used to study the different interactions in five newly synthesized biologically active triazolothiadiazole derivatives.